

BROADBAND GROUND MOTION SYNTHESIS VIA GENERATIVE ADVERSARIAL NEURAL OPERATORS: DEVELOPMENT AND VALIDATION *

 **Yaozhong Shi**

Division of Engineering and Applied Sciences
California Institute of Technology
Pasadena, California, U.S.A.
yshi5@caltech.edu

 **Grigorios Lavrentiadis**

Division of Engineering and Applied Sciences
California Institute of Technology
Pasadena, California, U.S.A.
glavrent@caltech.edu

 **Domniki Asimaki**

Division of Engineering and Applied Sciences
California Institute of Technology
Pasadena, California, U.S.A.
domniki@caltech.edu

 **Zachary E. Ross**

Seismological Laboratory
California Institute of Technology
Pasadena, California, U.S.A.
zross@caltech.edu

 **Kamyar Azizzadenesheli**

NVIDIA Corporation
Santa Clara, California, U.S.A.
kamyara@nvidia.com

ABSTRACT

We present a data-driven framework for ground-motion synthesis that generates three-component acceleration time histories conditioned on moment magnitude (M), rupture distance (R_{rup}), time-average shear-wave velocity at the top 30m (V_{S30}), and style of faulting. We use a Generative Adversarial Neural Operator (GANO), a resolution invariant architecture that guarantees model training independent of the data sampling frequency. We first present the conditional ground-motion synthesis algorithm (cGM-GANO) and discuss its advantages compared to previous work. We next train cGM-GANO on simulated ground motions generated by the Southern California Earthquake Center Broadband Platform (BBP) and on recorded KiK-net data and show that the model can learn the overall magnitude, distance, and V_{S30} scaling of effective amplitude spectra (EAS) ordinates and pseudo-spectral accelerations (PSA). Results specifically show that cGM-GANO produces consistent median scaling with the training data for the corresponding tectonic environments over a wide range of frequencies for scenarios with sufficient data coverage. For the BBP dataset, cGM-GANO cannot learn the ground motion scaling of the stochastic frequency components ($f > 1Hz$); for the KiK-net dataset, the largest misfit is observed at short distances ($R_{rup} < 50km$) and for soft soil conditions ($V_{S30} < 200m/s$) due to the scarcity of such data. Except for these conditions, the aleatory variability of EAS and PSA are captured reasonably well. Lastly, cGM-GANO produces similar median scaling to traditional GMMs for frequencies greater than 1Hz for both PSA and EAS but underestimates the aleatory variability of EAS. Discrepancies in the comparisons between the synthetic ground motions and GMMs are attributed to inconsistencies between the training dataset and the datasets used in GMM development. Our pilot study demonstrates GANO's potential for efficient synthesis of broad-band ground motions.

* Accepted by *Bulletin of the Seismological Society of America*

1 Introduction

The demand for reliable ground motion time histories for seismic analysis is growing, yet there are still not enough records of large earthquakes covering the desired range of source, path, and site characteristics (Katsanos et al., 2010), in particular at near-source ground motions or on very soft site conditions. In order to resolve the limitations caused by data scarcity, ground motion records are usually selected and scaled in the time domain or adjusted in the frequency domain to satisfy specified intensity measurements or frequency content (Goulet et al., 2008; Rezaeian and Der Kiureghian, 2012). However, scaling or modification of records that is not based on physics may only scale some intensities or frequency measures while leaving other elements unaltered, leading to unrealistic ground motions (Naeim and Lew, 1995; Luco and Bazzurro, 2007; Baker et al., 2021). Additionally, most of the scaling and spectrum matching techniques only modify the two horizontal components making them unsuitable for structural models that are sensitive to all three components (Bhosale et al., 2017).

Methods for synthesizing ground motions offer an alternative solution by directly generating ground motions for the scenarios of interest. These methods can be broadly grouped into “physics-based” numerical simulations and “stochastic-based” approaches, depending on whether the process of generating synthetic waveforms involves physics (Douglas and Aochi, 2008). In general, stochastic-based methods for ground motion generation involve modifying white noise to emulate specific ground motion characteristics (Dabaghi and Der Kiureghian, 2017; Baglio et al., 2023; Sabetta et al., 2021; Burks and Baker, 2014), while physics-based numerical simulations rely on modeling the physics that govern earthquakes, such as wave propagation and seismic source radiation to generate ground motions for a scenario of interest (McCallen et al., 2021; Paolucci et al., 2021; Touhami et al., 2022).

Physics-based methods have the advantage of generating complex path and site effects, but they are still far from being incorporated in routine engineering applications due to the following reasons: (1) Such approaches demand in-depth knowledge of sources, paths, and site effects, which are usually unavailable for most engineering purposes. (Causse et al., 2008; Frankel, 2009; Rezaeian and Der Kiureghian, 2012). (2) they require expensive computations to provide sufficient high-resolution frequency. Nowadays, with the assistance of supercomputers, it is possible to synthesize broadband ground motions up to $10Hz$ (Rodgers et al., 2020); however, such computational resources are not available for most engineering projects. (3) Even with earthquake simulations capable of generating high-frequency ground motions, the accuracy and spatiotemporal variability will continue to lag behind the input model accuracy for source physics, crustal complexity, nonlinear site response, and other constituent elements of simulating earthquakes end-to-end. (4) To achieve the desired frequency resolution, the generated ground motions may be applicable only to a limited range of site conditions due to the application of minimum V_S threshold for wave propagation or the omission of non-linear effects. For instance, to achieve computational efficiency, some physics-based methods impose a V_S lower limit at 500 m/s, which means such methods cannot accurately simulate strong motions at soil sites (Pitarka et al., 2013).

Stochastic methods take a different approach to generating ground motions for engineering applications. The main advantages are that: (1) the source, site, and path scaling terms can be determined from empirical data and can simply be combined to generate the desired ground motions (Hanks and McGuire, 1981; Boore, 1983, 2003), and (2) they are computationally efficient. At the same time, the main limitations of stochastic methods are (1) Such methods are based on the reconstruction of particular features, such as pseudo-spectral accelerations (PSA) (Tavakoli and Pezeshk, 2005) or pseudo-spectral velocity (PSV) (Boore, 2003) without taking physics into account to fully characterize the ground motion. (2) Due to their inability to properly represent P, S, surface-wave modes, and polarization, stochastic methods cannot be used to produce coherent 3-component waveforms with multiple arrivals and coda that are representative of real ground motions (Graves and Pitarka, 2010). (3) They tend to underestimate the correlation between amplitudes at different frequencies compared to observed motions, which underestimates the variability in the building response and can have an impact on the calculated risk (Stafford, 2017; Bayless and Abrahamson, 2019).

In both stochastic and physics-based models, a source of model uncertainty arises from the approximate representation of unresolved processes through parameterized functional forms. Model errors can be reduced to a certain degree through targeted data collection, leading –for example– to an improved spatial resolution of 3D velocity models in physics-based simulations, but they cannot be eliminated because there is no resolution separation between resolved and unresolved processes. At the same time, functional parameterization is often necessary for robust model extrapolation, especially outside the range of available data. However, for applications with dense data coverage and emphasis on interpolation (i.e., surrogate modeling of hybrid empirical-numerical strong motion datasets), machine learning models offer a fundamentally different approach to reduce model uncertainty: they parameterize the complex, nonlinear sub-resolution processes directly from the data that describe those processes using well-defined optimization rules (Gagne et al., 2020; Kong et al., 2019). With the growth of available high-quality strong ground motion data and the explosion of modern machine learning algorithms, generating realistic ground motions that span the broadband range of engineering interest ($\sim 0.1 - 25Hz$) is no longer a far-reaching goal.

The types of stochastic methods mentioned previously are not data-driven, (i.e., they are not generative models learned from data). However, major advances in machine learning have been made in the last decade on the topic of deep generative models, in which the goal is to learn an unknown data distribution given a large dataset for training. Generative adversarial networks, or GANs (Goodfellow et al., 2014), are a class of generative models well suited for time-series synthesis. GANs draw samples from random distributions to generate new data that mimic an existing sample. Carefully designed GANs have uncovered and replicated the properties of time series in various fields such as finance, medicine, and seismology, including ground motion synthesis for earthquake early warning. Among others, Wang et al. (2019) and Wang (2021a) generated realistic seismic signals for training of early warning systems; (Li and Ku, 2020) also proposed a GAN-based method to artificially generate time series that resemble realistic seismic signals for early warning system training; Gatti and Clouteau (2020) used GANs to extract high frequency features from ground motion records and use them to enhance ground motion simulated time series; Matinfar et al. (2023) used GANs to synthesize ground motion acceleration time series compatible with a given target design spectrum; Florez et al. (2022) used GAN to synthesize realistic three-component accelerograms conditioned on a set of continuous physical variables (magnitude, distance, and shear wave velocity) and statistically evaluated the quality of the signals using common engineering ground-motion intensity measures; while Esfahani et al. (2023), inspired by Florez et al. (2022), simulated non-stationary ground-motion recordings leveraging information contained in the frequency domain and incorporating physics-based knowledge such magnitude and distance. For a detailed overview of the use of GANs in earthquake engineering fields, the reader is referred to Marano et al. (2023).

In this paper, we use a new class of generative models – a Generative Adversarial Neural Operator (GANO) (Rahman, 2022a) with the ultimate goal of building a framework that synthesizes ground motions for engineering applications. We first present the ground-motion synthesis algorithm and discuss its advantages compared to previous work. We next evaluate the GANO framework using noiseless ground motions simulated by the Southern California Earthquake Center (SCEC) Broadband Platform (BBP) (Maechling et al., 2014), and finally validate it by training it on three-component acceleration time histories from a strong-motion dataset processed from the Kik-Net network in Japan. In both applications, the generated ground motions are conditioned on moment magnitude (M), closest-point-on-the-rupture to site distance (R_{rup}). Additionally, for the BBP dataset the style of faulting (strike-slip or reverse event) was included as a conditional parameter, while for the Kik-Net dataset, the time average shear wave velocity at the top 30m (V_{S30}) and tectonic environment type (subduction or shallow crustal event) were the conditional variables. Lastly, we assess the performance of our model through residual analysis and through a comparison with published GMMs. While still in progress, quantitative analyses show that our GANO-generated ground motion model can overall reproduce realistic ground motion time histories with a broad range of frequencies (0.1~30Hz) for horizontal and vertical components and can approximate the variability in the empirical Kik-net dataset.

2 Methods

2.1 Neural Operators

The classical development of neural networks has primarily focused on learning mappings between finite-dimensional Euclidean spaces or finite sets. Neural operators were introduced as a generalization of neural networks, intended to learn mappings between continuous function spaces from finite input-output pairs (Li et al., 2020, 2021). Learning mappings between function spaces has shown great success at efficiently solving complex partial differential equations (PDEs). For instance, Pathak et al. (2022); Wen et al. (2022); Yang et al. (2021), have shown that neural operators can efficiently reproduce simulations governed by PDEs in problems of weather forecasting, CO₂ injection, and wave propagation in solids to name a few.

Neural operators can be understood as mappings between infinite-dimensional function spaces. Suppose, for instance, that there is a non-linear mapping $\mathcal{F}: \mathcal{A} \rightarrow \mathcal{U}$, where \mathcal{A} is the input and \mathcal{U} is the output function space. The neural operator approximates the solution operator \mathcal{F} using a fixed set of parameters ($\mathcal{F}_\theta \approx \mathcal{F}$) that provide a continuous representation of \mathcal{U} in the function space. Kovachki et al. (2023) formally established that neural operator models with a fixed number of parameters satisfy discretization invariance; and further showed that they are universal approximators of continuous operators, namely, can uniformly approximate any continuous operator defined on a compact set of normed vector spaces. According to Kovachki et al. (2023), neural operators are the only known class of models that guarantee both discretization-invariance and universal approximation.

A computationally efficient variant of Neural Operators particularly suited for wave propagation (and synthesis) are Fourier Neural Operators (FNO) (Li et al., 2021), whereby the representation and parameterization of the neural operator kernel are formulated in the Fourier space. Despite the advantages in terms of efficiency and accuracy, FNOs, which according to Kovachki et al. (2023) *achieved the best numerical performance of all the numerical experiments*, are fully connected networks, and as such, the memory requirements associated with their training can be significant. Inspired by

the U-net architecture (Ronneberger et al., 2015), Rahman (2022b) proposed an architecture referred to as the U-shaped Neural Operator (U-NO), which relies on gradually compressing and decoding information to alleviate issues associated with excess memory requirements. U-NO has the advantage of faster training and less memory requirements compared to standard FNO.

2.2 Generative Adversarial Neural Operators (GANO)

Generative Adversarial Neural Operators (GANO) generalize the Generative Adversarial Network (GAN) framework (Rahman, 2022a), which is one of the most prominent paradigms in machine learning for analyzing unsupervised data. While GANs are successful generative models with a wide range of theoretical developments (Arjovsky et al., 2017), their empirical success has been only in finite-dimensional data regimes. In fact, there has been little progress in developing generative models for infinite-dimensional spaces and function spaces, which limited the use of GANs for learning functional data (i.e., data on irregular grids in space and time), which is often the case in the fields of science and engineering.

A GANO framework consists of a neural operator generator and a discriminator functional (i.e., a neural operator followed by an integral function). The generator uses Gaussian Random Fields (GRFs) or any predefined probability function as input and outputs a function sample. The discriminator accepts as input real or synthetic data and returns a scalar (score). The objective function, namely the score generated by the discriminator, is used for the loss function. Rahman (2022a) devised the GANO framework by i) generalizing the Wasserstein GAN setting (Arjovsky et al., 2017) to infinite dimension space, and ii) using the generalized Wasserstein distance and a gradient penalty as regularization terms to make the models more stable and less sensitive to the tuning of their hyperparameters.

2.3 Conditional Ground Motion GANO (cGM-GANO)

In this paper, we present a conditional GANO architecture designed to generate realistic 3-component acceleration time histories; we will refer to the architecture in the following sections as cGM-GANO. The architecture presented here has been trained on four conditional variables: the moment magnitude (M), the closest-point-on-the-rupture to site distance (R_{rup}), the time-averaged shear wave velocity in the top 30m (V_{S30}), and the style of faulting or tectonic environment (f_{type}). f_{type} is used to differentiate between strike-slip ($f_{type} = 1$) and reverse ($f_{type} = 0$) events for the BPP data set, or shallow crustal ($f_{type} = 1$) and subduction ($f_{type} = 0$) events for the Kik-net data set. Given a vector of the aforementioned parameters, it generates 3-component acceleration time series (Fig 1). We should note here that the selection of four variables is a modeling decision and could be replaced with any number of conditional variables, provided that there is a sufficiently large dataset for GANO to learn the effect of the different parameters.

To design cGM-GANO, we implemented the U-NO architecture in a GANO framework, as outlined in the previous section. cGM-GANO consists of a generator and discriminator trained in a min-max adversarial game (Fig. 2). We should note here that the training database of ground motions spans 3-4 orders of magnitude of PGA amplitude; as such, acceleration time series needed to be normalized to a common amplitude scale to ensure that there was no loss of information (Goodfellow et al., 2016; Wu and He, 2018) so that small events are not interpreted as noise. The normalization constants for each channel of the three component time series are also *learned* and recovered when the trained generator is called to synthesize a conditional ground motion scenario. The input to the trained generator consists of two sets of one-dimensional (1D) discretized functions: (i) a 1D Gaussian Random Field (Gaussian Process), which is stochastic (ii) and a set of constant functions that are used to convert the input parameters (M , R_{rup} , V_{S30} , f_{type}) to a measurable function. The output includes the 3-component normalized ground motion waveforms and three normalization constants, in this case, the peak amplitudes associated with the normalized waveforms.

Compared to the previous work by the authors (Florez et al., 2022), the important advantage of GANOs that pertains to the problem of ground motion synthesis is their resolution and discretization invariance (Kovachki et al., 2021): the input function to the generator can be expressed with an arbitrary discretization (i.e., a dataset of time series sampled at various frequencies), yet the generated output is a function, which can be queried at any (i.e., frequency) resolution. These properties follow the recent advancements in operator learning that generalize neural networks (and thus GANs) that only operate on a fixed resolution (Kovachki et al., 2021); specifically in Florez et al. (2022), the input to the GAN was a sample from a finite-dimensional multivariate random variable and the output was a finite-dimensional object that could be queried only at a predetermined time-frequency resolution.

Additionally, GANOs can learn probability measures on function spaces, in contrast to GANs, a difference that has been shown to avoid the mode collapse issues seen in GANs when the training data is generated from a mixture of GRFs (GANO reliably recovers the modes included in the mixture). For more information related to mode collapse and the strategies of hyperparameter tuning that have been developed to avoid it, as well as issues associated with training stability and mode entanglement of GANs, the reader is referred to Rahman (2022a); Wang (2021b); Abdal et al. (2020).

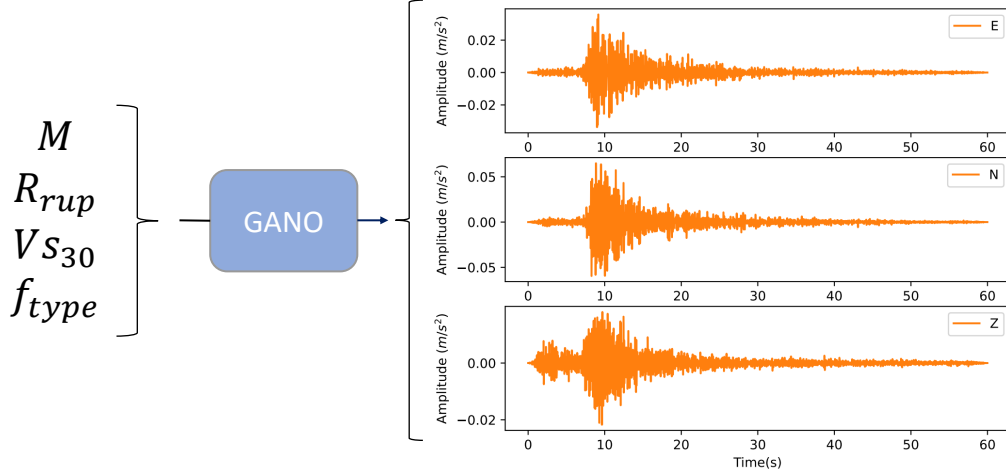


Figure 1: Schematic of GANO input-output structure used in this work: given a set of conditional variables (left), the trained GANO (middle) produces three-component acceleration time series (right).

In what follows, we present the cGM-GANO training strategy, as well as the verification framework using simulated (noise-free) ground motions, and the validation framework using strong motion recordings from the Japanese strong motion network Kik-Net and empirical ground motion models. By contrast to Florez et al. (2022), we here train GANO using velocity time series and then differentiate the generated ground motions to compute the target 3-component acceleration time series. Learning the acceleration time integral is equivalent to learning a linear filter of the target time series that balances the low and high frequencies. This effect is better described with (1) where for non-zero frequencies, the integral amplifies low-frequency components (for $\omega \leq 1$) and suppresses the high-frequency components (for $\omega \geq 1$). An example of the frequency content comparison between acceleration, velocity, and displacement is presented in the electronic supplement Fig S1.

$$\int_0^t f(t) \xleftrightarrow{FT} \frac{F(\omega)}{j\omega} \quad (1)$$

2.4 Residual Analysis and Comparison to Empirical Ground Motion Models

The statistical evaluation of the generated ground motions was performed (i) by comparing the PSA and FAS, for BBP dataset, or EAS, for Kik-net dataset, ordinates of the observed and synthetically generated ground motions for specific scenario bins and (ii) by performing residual analysis of the PSA and FAS or EAS of the training and testing datasets, for both the horizontal and vertical directions. For the horizontal component, PSA was calculated as the rotation-independent 5%-damped response spectra (RotD50) for periods in the 0.01 – 10sec range (Boore, 2006, 2010) using a modified GPU parallel computation version of the PyrotD (Kottke, 2018) python library, while in the vertical direction PSA was calculated as 5%-damped response spectrum of the vertical component. The horizontal FAS was calculated as the power mean spectrum of the two horizontal components:

$$A_h(f) = \sqrt{\frac{1}{2} (A_{h1}(f)^2 + A_{h2}(f)^2)} \quad (2)$$

where, $A_{h1}(f)$ and $A_{h2}(f)$ are the FAS of the two horizontal components at frequency f . The calculation of the horizontal EAS followed the recommendations of Kottke et al. (2021), smoothing the power-mean FAS through a Konno and Ohmachi (1998) smoothing window (Equation 3) with bandwidth, $b_w = 0.0333$. The vertical FAS was calculated directly from the vertical component, and the vertical EAS was smoothed with the Konno-Ohmachi filter.

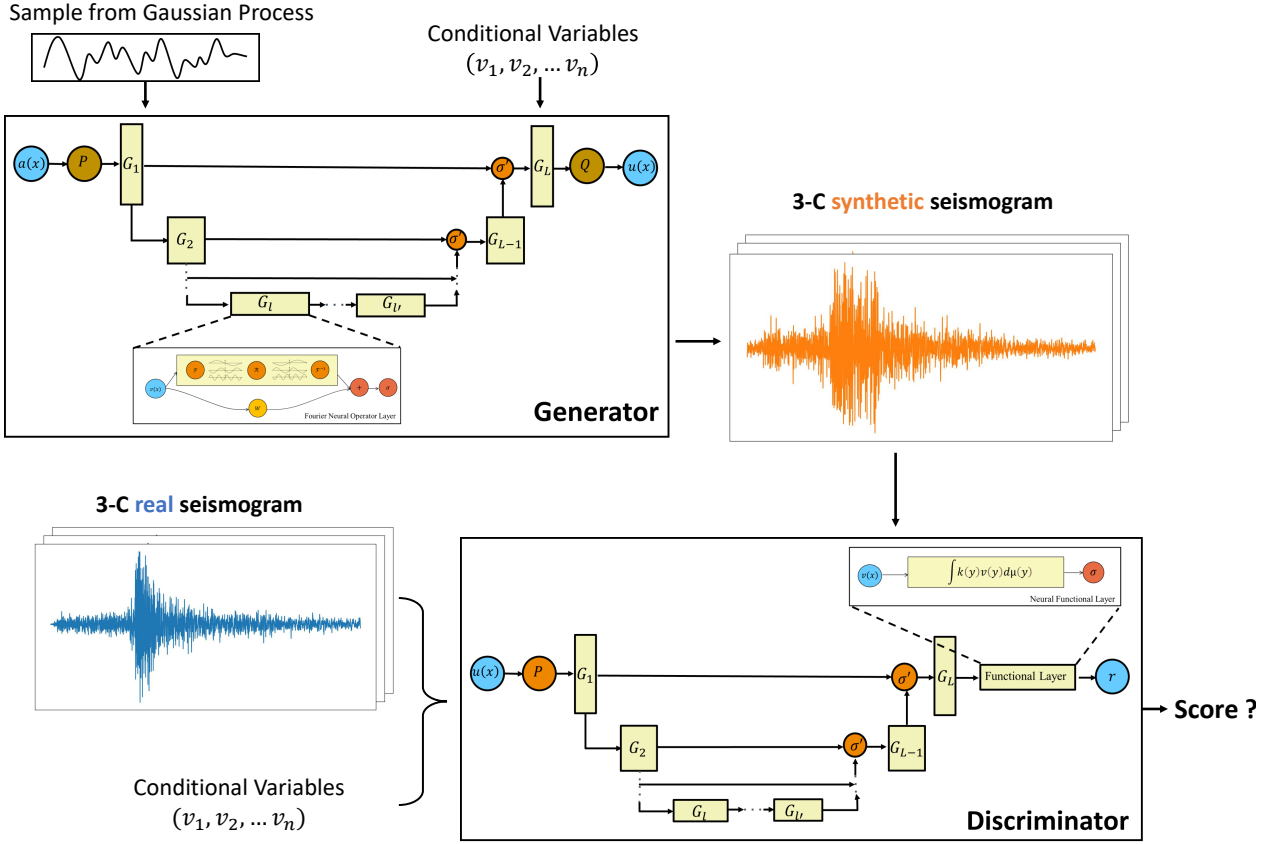


Figure 2: Schematic of cGM-GANO architecture, and generator - discriminator interaction. The input conditional variables are M , R_{rup} , V_{S30} and f_{type} . The input function for the generator is finite duration Gaussian random field sample while the output is the normalized three-component acceleration time series and three PGAs. The input function of the discriminator are the real or synthetic three-component acceleration time series while the output is score evaluating the realism of the input ground motions.

$$b = 2\pi/b_w \quad (3)$$

$$W(f) = \left(\frac{\sin(b \ln(f/f_c))}{b \ln(f/f_c)} \right)^4 \quad (4)$$

The residual analysis was performed by comparing the observed intensity measures (IM) with the distribution of the synthetic ground motion IM , within the useable frequency range of the observed ground motions. The comparison is performed by: (i) generating 100 synthetic 3-component realizations with the same $(M, R_{rup}, V_{S30}, f_{type})$ conditional variable values of the observed ground motion, (ii) computing the relevant IM from the observed and synthetic ground motions ($IM^{observed}$, $IM^{cGM-GANO}$, respectively), (iii) calculating the mean and standard deviation of $IM^{cGM-GANO}$ in log space, and (iv) computing the normalized model residual, ϵ , for each observation as:

$$\epsilon = \frac{\ln(IM^{observed}) - \text{mean}(\ln(IM^{cGM-GANO}))}{\text{std}(\ln(IM^{cGM-GANO}))} \quad (5)$$

this way the mean of ϵ quantifies bias and the standard deviation of ϵ the variability of the predictive model with respect to the data. A zero mean ϵ indicates that the ensemble of synthetic ground motions is unbiased with respect to the observations, and a unit ϵ standard deviation, or a two-unit width between the 16th and 84th ϵ percentile, suggests that the variability of the synthetic ground motion ensemble is consistent with the variability of the empirical dataset.

Since the BBP waveforms are considered noiseless, the entire frequency content of the ground motion was part of the useable frequency range. Kik-net ground motions, on the other hand, were filtered based on the noise-to-signal ratio (Bahrapouri et al., 2021). In this case, the useable frequency range is defined as:

$$\text{Lowest usable frequency (LUF)} = 1.25\max(HPF_{H1}, HPF_{H2}, HPF_V) \quad (6)$$

$$\text{Highest usable frequency (HUF)} = 0.8\min(LPF_{H1}, LPF_{H2}, LPF_V) \quad (7)$$

where HPF_{H1} , HPF_{H2} , and HPF_V are the corner frequencies of the high pass filter for the two horizontal and vertical component, while LPF_{H1} , LPF_{H2} , LPF_V are the corner frequencies for the low pass filter of the same components. The calculation of residuals was performed only within the usable frequency range to remove the effect of filtering

Lastly, we compared the scaling predicted by cGM-GANO against representative GMMs for the KiK-net dataset as part of our ongoing effort to develop a tool for efficient ground motion synthesis for engineering applications. Comparisons were performed against published PSA and EAS models such as the NGA-West2 GMMs (Abrahamson et al., 2014) and BA18 (Bayless and Abrahamson, 2019) for the shallow crustal events and BCHydro (Abrahamson et al., 2016) for the subduction events.

3 Training with Simulated Ground Motions: Verification

We first verified our cGM-GANO architecture by training it on simulated ground motion time series generated using the SCEC BBP, a collection of open-source scientific software modules that can simulate broadband ($0 \sim 20Hz$) ground motions for earthquakes at regional scales (Maechling et al., 2014).

The goal of this exercise was to verify that cGM-GANO is able to assimilate noiseless ground motion training data to reproduce the median scaling and aleatory variability of the simulations. Verifying the reasonableness of the simulated ground motions, however, was outside the scope of this study. This exercise was conducted first, before testing cGM-GANO on observed ground motions, as it offered a simpler learning environment. The BBP-generated ground motions do not require filtering and baseline correction, reducing the number of factors affecting the waveforms, and the uniform site conditions across the ensemble of simulated scenarios reduce the number of conditional variables that cGM-GANO was called to learn.

For this study, we used a dataset developed on BBP v17.3.0. following the Graves and Pitarka (2015) simulation module (BBP-GP). This module is a hybrid approach that combines low-frequency (often referred to as deterministic) and high-frequency (often referred to as stochastic) motions computed with different methods into a single broadband response. The database was developed by Shi (2019) in collaboration with the BBP-GP developer, Robert Graves (pers. communication), and it contains 113 events ranging from M 5.5 to 7.2 on strike-slip and from M 7.0 to 7.2 on reverse faults, recorded at stations on reference site conditions ($V_{s30} = 760$ m/s), at rupture distances between 0 to 200 km. The database contains 6704 acceleration time histories: each record has 3-component 40s waveforms sampled at 100Hz. The magnitude-distance-PGA distribution of the data is shown in Fig 3. A representative illustration of the fault and stations' locations is shown in Fig S2 in the electronic supplement.

In this case, the cGM-GANO was trained conditioned on the moment magnitude (M), on the closest-point-on-the-rupture to site distance (R_{rup}), and on the fault type (f_{type} , strike-slip or reverse).

Fig. 4 compares the FAS and PSA spectra of BBP simulated and GANO-generated 3-component waveforms for M 7.0 strike-slip and reverse events at 10 km rupture distance. The comparison of the FAS and PSA ordinates is encouraging, especially in the long period, short frequency regime, where both the mean and standard deviation are in agreement. In particular, one can observe that the standard deviation of the two data sets converges for frequencies smaller than $f < 1Hz$ ($T > 1sec$), while for higher frequencies, the cGM-GANO-generated time series have systematically higher variability. Our working hypothesis is that the discontinuity occurs at $f = 1Hz$, the cross-over frequency between the low- and high-frequency methods in the BBP-GP hybrid module, because cGM-GANO cannot learn the stochastic high-frequency method and resorts to carrying over the learned physics-based solution of $f < 1Hz$ into the higher frequency range. One reason for this might be that GANO can only learn distributions over functions that are square-integrable, and the stochastic generation method used in the BBP does not necessarily satisfy this property. Representative waveforms from both the BPP and cGM-GANO are also depicted in the electronic supplement (Fig S3), showing that the synthetic time series manifest realistic features, such as P-, S-, and coda wave arrivals, as well as time history envelopes consistent with the simulated ground motions.

Next, we test the capabilities of cGM-GANO to learn the magnitude and distance scaling in sparsely sampled regions of the training dataset. Fig. 5 shows that the BBP training database by Shi (2019) has no reverse event records (here, depicted by the dot markers) for small magnitude at distances 20 – 40km, or for magnitudes M6.9 – 7.1 at large

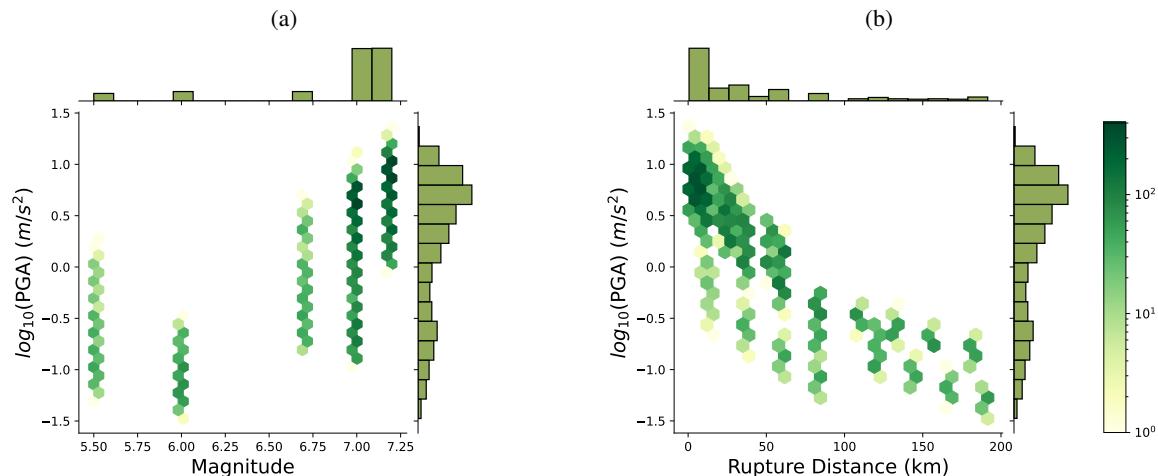


Figure 3: Data distribution of BBP dataset. Subfigures (a) and (b) show crossplot between $\log_{10}(\text{PGA})$ and magnitude and rupture distance, respectively

distances ($\geq 50\text{km}$). Still, the cGM-GANO was trained using data from both reverse and strike-slip events, each appropriately tagged. The example in the figure suggests that the model has, in part, inferred the median magnitude and distance scaling of the reverse style faulting from the data ensemble training, transferring the information across faulting styles. At the same time, however, the variability of cGM-GANO is larger than the BBP data in the densely sampled regions of the training dataset (for example, $M6.9 - 7.1$ far-field strike-slip as well as near-field reverse) where one would expect the variability to be best captured.

Lastly, we examined the degree to which cGM-GANO can recover the frequency domain characteristics of the BBP simulated ground motions through a residual analysis. Results for the horizontal and vertical components of the EAS and RotD50 residuals are shown in Fig 6, separately for the strike-slip and the reverse simulated events. The cGM-GANO results for the horizontal EAS components for both types of ruptures show discontinuities at 1Hz. The mean and aleatory variability are captured reasonably well for both strike-slip and reverse events in the low-frequency range ($f \leq 1\text{Hz}$). In the high-frequency range ($f > 1\text{Hz}$), the mean is captured reasonably well, but the aleatory variability is underestimated for strike-slip events, and there is a noticeable bias in the mean and underestimation of the variability for reverse events. The RotD50 spectral accelerations show a slight constant positive bias across the period range for both styles of faulting. The difference between EAS and RotD50 residual distributions is attributed to the unsuitable inter-frequency correlation of the synthetic ground motions that is influenced by the stochastic component of the training dataset (Electronic Supplement Fig S4); further investigation is needed, nonetheless, to find the exact cause of the mismatch between the bias and variability of EAS and PSA in the various frequency-period ranges.

Our working hypothesis is that verification of cGM-GANO using BBP simulations, which are synthesized by two separate processes, is compromised when the neural operator attempts to recover the entire frequency range as if it were the solution of the wave equation for propagation in a continuum. Whether the identified biases in the aforementioned figures stem from the hybrid BBP-GP method and the difficulties associated with training neural operators on stochastic data; or it is evidence that more training data is necessary to reliably recover the median and standard deviation scaling relationships across the entire dataset, is still being debated. More extensive validation is currently being carried out by the authors to confirm this claim, including the simulation of large-magnitude, near-field reverse faulting events to confirm the aforementioned recovered scaling. These results, along with the foregoing sections, however, point to the possibility of using cGM-GANO in the future to fill sparsely sampled regions of observational datasets used to develop GMMs with defensible, realistic, 3-component ground motion time series appropriate for engineering applications.

4 Training with Recorded Ground Motions: Verification and Validation

In this section, we evaluated the performance of cGM-GANO by training it on a ground motion dataset compiled from the Japanese Strong Motion Network KiK-net (NIED, 2019). The compiled KiK-net dataset included 42481 strong ground motions sampled at 100Hz from 1985 events, 620 shallow crustal and 1365 subduction events, collected over a period of 20 years (from 1997 to 2017) at 613 stations. For the data preprocessing, we used the method described in Bahrampouri et al. (2021), which comprises of the following steps: (i) identify the filter corner frequencies for each

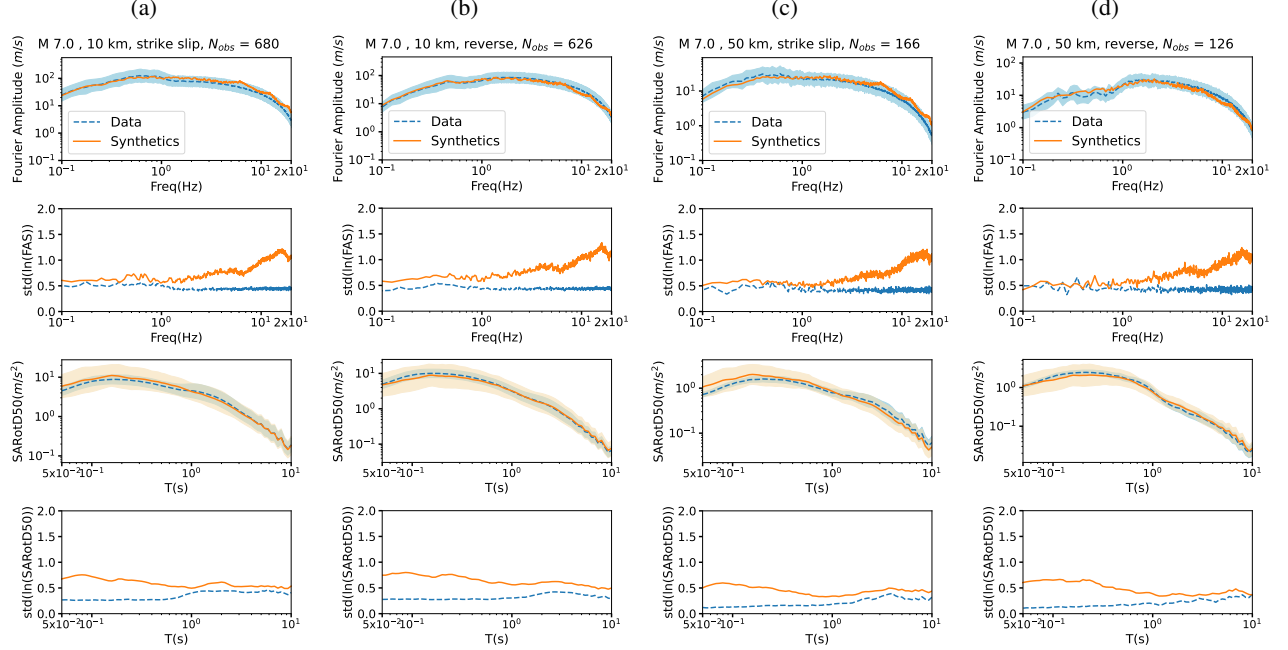


Figure 4: Scenario event comparisons for cGM-GANO trained on the BBP dataset. Each vertical sub-panel depicts the Fourier Amplitude Spectrum (FAS), aleatory standard deviation of FAS, Rotd50 Pseudo-spectral acceleration (PSA) spectrum, and aleatory standard deviation of Rotd50. The title of each plot corresponds to the midpoint of each bin, and N_{obs} is the number of observed records within each bin. The lines represent the mean in log space of the horizontal components of the synthetic (solid line) or BBP (dashed line) data, while the shaded zone represents the 16th to 84th percentile range.

record based on noise windows, and (ii) detect the P- and S-wave arrivals. We ensured that each time history contained the ground motion from a single event, and we used a fixed duration of 60sec for training, starting from the onset of the P wave. The choice of a fixed duration window stems from FNO requirements that we used in our architecture. Prior to training, we detrended and baseline-corrected the KiK-net ground motions to ensure that the displacement, velocity, and acceleration are zero at the end of the 60sec. The same baseline correction was applied on the cGM-GANO generated ground motion time series before the validation tests described below.

The conditional parameters for the KiK-net dataset (M , R_{rup} , V_{S30} , and f_{type}) were obtained from Bahrapouri et al. (2021); M ranges from 4.5 to 8.0, R_{rup} from 0 to 300 km, V_{S30} from 100 to 1100 m/s, and the tectonic environment is subduction or shallow crustal. Figure 7 shows the magnitude, distance, and V_{S30} distribution of the compiled data, which is primarily comprised of small-to-moderate events recorded at distances $R_{rup} \geq 50$ km, on moderate stiffness sites. Only 1.6% of the dataset ground motions corresponded to events with $M \geq 7.0$, 2.8% of records have rupture distances less than $R_{rup} \leq 50$ km, and 2.7% of the ground round motions were recorded on stations with $V_{S30} < 200$ m/sec.

For training purposes, the KiK-net dataset was randomly divided into 90% training data and 10% testing data, not used in training. In what follows, we present verification results against the entire database, while validation results based on the testing dataset alone are provided in the electronic supplement (Fig S5). Both the entire and testing datasets show similar trends, indicating no overfitting on the training dataset. It was decided to include the comparison with the entire dataset in the manuscript for more robust magnitude, rupture distance, V_{S30} scaling, and individual scenario comparisons.

Fig 8 shows a visual comparison between randomly sampled observed time series for different M , R_{rup} , V_{S30} combinations and the corresponding cGM-GANO random realizations for the same scenarios. This comparison is intended to show that the generated waveforms are comparable in amplitude, duration and phase arrival with the recorded ground motions.

Fig. 9 compares the frequency domain statistics of the observed and cGM-GANO generated time-series belonging to the same M , R_{rup} , V_{S30} bin. Although neural operators map function spaces and by definition have continuous

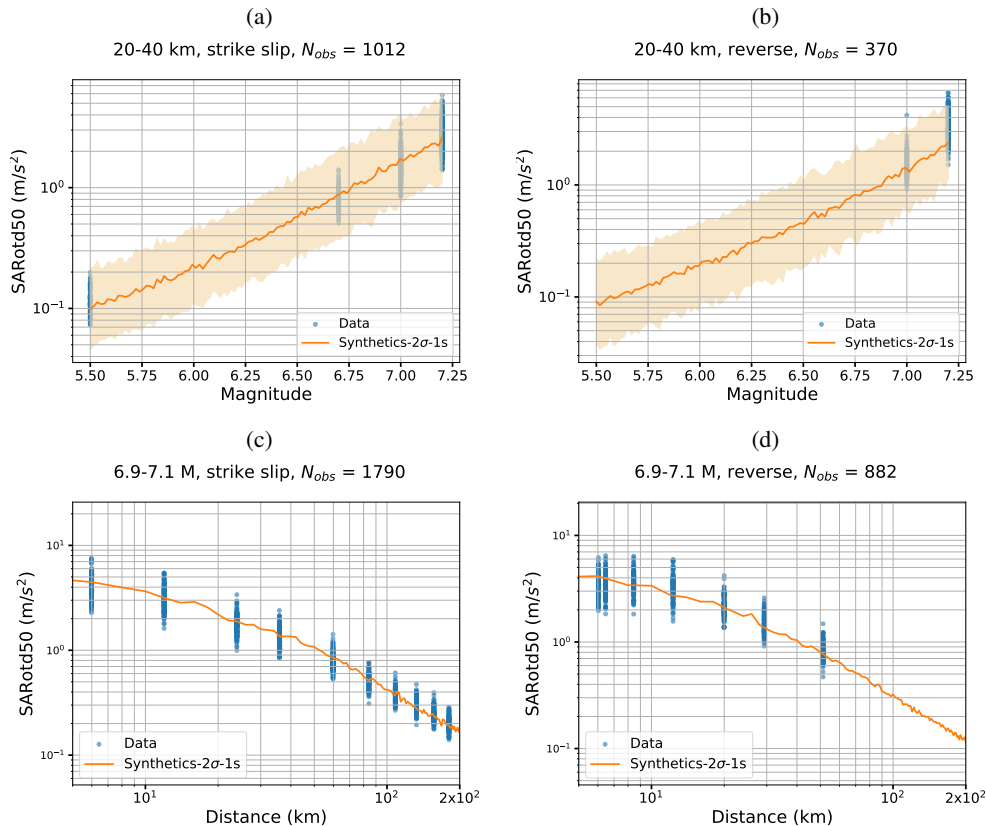


Figure 5: Comparison of cGM-GANO magnitude and distance scaling with BBP dataset for PSA RotD50($T=1$ s). Solid lines represent the mean scaling in log space. The shaded region shows the 2^{nd} to 98^{th} percentile of aleatory variability. Solid dots correspond to the training data.

input spaces (i.e., conditional variables), for the validation we binned the data in windows of increment $M = 0.2$, $R_{rup} = 20\text{km}$ and $V_{S30} = 100\text{ m/s}$ to ensure that the number of records in each bin would provide statistically significant results for comparison purposes. We successively generated cGM-GANO time-series for each scenario in each bin to create a database of synthetic ground motions for the same scenarios as the observations in each bin. The statistics of the two datasets are compared for representative bins in Fig. 9. For the examples shown, cGM-GANO recovers the mean and aleatory variability of the FAS in the frequency range between ~ 0.5 Hz and 30 Hz. Similarly, cGM-GANO recovers the mean and aleatory variability of PSA RotD50 in most cases; exceptions such as scenario (e) for periods shorter than $T = 0.2\text{sec}$, or scenario (f) for periods longer than $T = 1\text{sec}$ which may stem from the small number of observations available in those bins (21 and 17 observations, respectively) and will be further investigated by the authors.

We successively examined the extent to which cGM-GANO can recover the M , R_{rup} , V_{S30} scaling of the ground motion observations for a given tectonic environment by means of residual analysis (for more information, see Section on Residual Analysis above). Results for the horizontal and vertical components of the EAS and RotD50 residuals are shown in Fig 10, separately for the subduction and the shallow crustal events. The cGM-GANO results of the horizontal EAS components for both tectonic environments are unbiased in the frequency range $\sim 0.3 - 20\text{Hz}$. The vertical components show similar behavior with a small increasing bias starting at 0.5Hz . The horizontal spectral accelerations are well captured in the $\sim 1 - 10\text{sec}$ period range and show small, nearly constant positive bias for shorter periods $T \leq 1\text{sec}$. The vertical spectral accelerations for both tectonic environments are well captured in the $T \geq 2\text{sec}$ period range, while for shorter periods, cGM-GANO shows significant bias. While encouraging, these results leave open questions about the frequency range where cGM-GANO can reliably recover the mean and aleatory variability of recorded ground motions and the factors that affect the reliability of the GANO model, which are further investigated by the authors.

The extent to which cGM-GANO recovers the ground motion scaling versus M , R_{rup} , V_{S30} is presented in Figs 11 and 12. The horizontal and vertical FAS residuals in subfigures 11 (a) and (c), and horizontal and vertical PSA residuals in

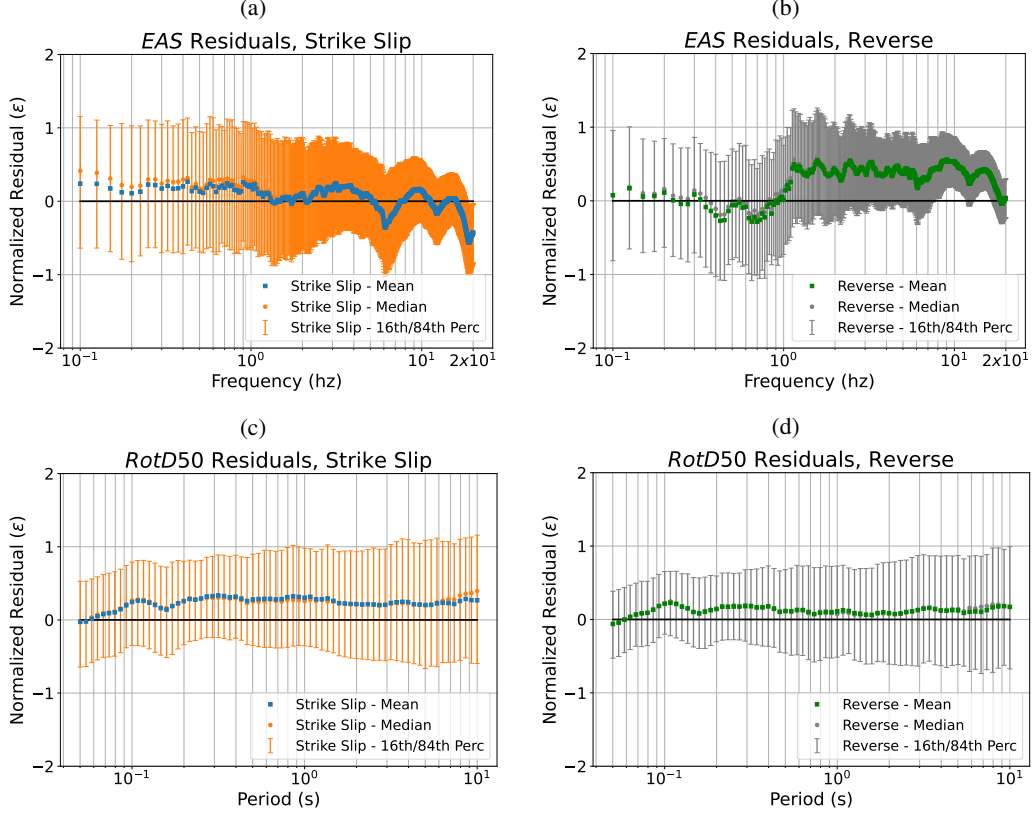


Figure 6: Residual plots of the BBP trained model. Subfigures (a) and (b) show the EAS residuals for strike-slip and reverse faults, respectively. Subfigures (c) and (d) show the RotD50 PSA residuals for strike-slip and reverse faults, respectively.

subfigures 12 (a) and (c) for $f = 5\text{Hz}$ ($T = 0.2\text{s}$) suggest that cGM-GANO can recover the median magnitude scaling of the ground motions. By contrast, cGM-GANO shows systematic positive bias when called to evaluate the median scaling against rupture distance, for $R_{rup} \leq 20\text{ km}$ (see Figs 11 and 12 (b) and (e)). Our working hypothesis is that the bias reflects the very small number of near-field observations (0.4% of the entire training dataset recorded at distance less than 20km), which may not be enough for the model to learn the ground motion characteristics in this regime. The cGM-GANO generated ground motion scaling with V_{S30} recovered in Figs 11 and 12 (c) and (f) shows negative bias for both FAS and RotD50 versus V_{S30} for sites with $V_{S30} \leq 200\text{ m/s}$. The bias in this V_{S30} range could be associated with the limited number of ground motion observations for soft soil sites within the KiK-net strong motion network (2.7% of the entire training dataset was recorded at sites with $V_{S30} \leq 200\text{ m/s}$.) Although this is not a negligible dataset of training ground motions, we hypothesize that training cGM-GANO to generate strong motions at soft sites would be associated with learning ground motion characteristics controlled by nonlinear effects, which are likely less pronounced for stiffer sites and thus less likely to be learned from the remainder of the dataset. This hypothesis is supported by the fact that the vertical component scaling with V_{S30} shows a small, nearly constant positive bias across the same V_{S30} range. The capability of cGM-GANO to learn the effects of nonlinear site response, given the appropriate size of training data and conditional variables, is the focus of a separate study undertaken by the authors. Considered strategies for this objective include augmenting the dataset with synthetic datasets that include non-linear effects and employing a weighting sampling, increasing the frequency of soft sites being sampled during training.

We also evaluated the inter-frequency correlation of the cGM-GANO-generated ground motion time series. Fig 13 shows the correlation of the RotD50 residuals between $T=1\text{s}$ and $T=0.2\text{s}$ or $T=2.0\text{s}$ for the entire KiK-net dataset. The Pearson correlation coefficient of residuals (ρ) at the period pairs T_1 and T_2 is also calculated as follows:

$$\rho_{\epsilon_{T_1}, \epsilon_{T_2}} = \frac{\text{cov}(\epsilon_{T_1}, \epsilon_{T_2})}{\sigma_{\epsilon_{T_1}} \sigma_{\epsilon_{T_2}}} \quad (8)$$

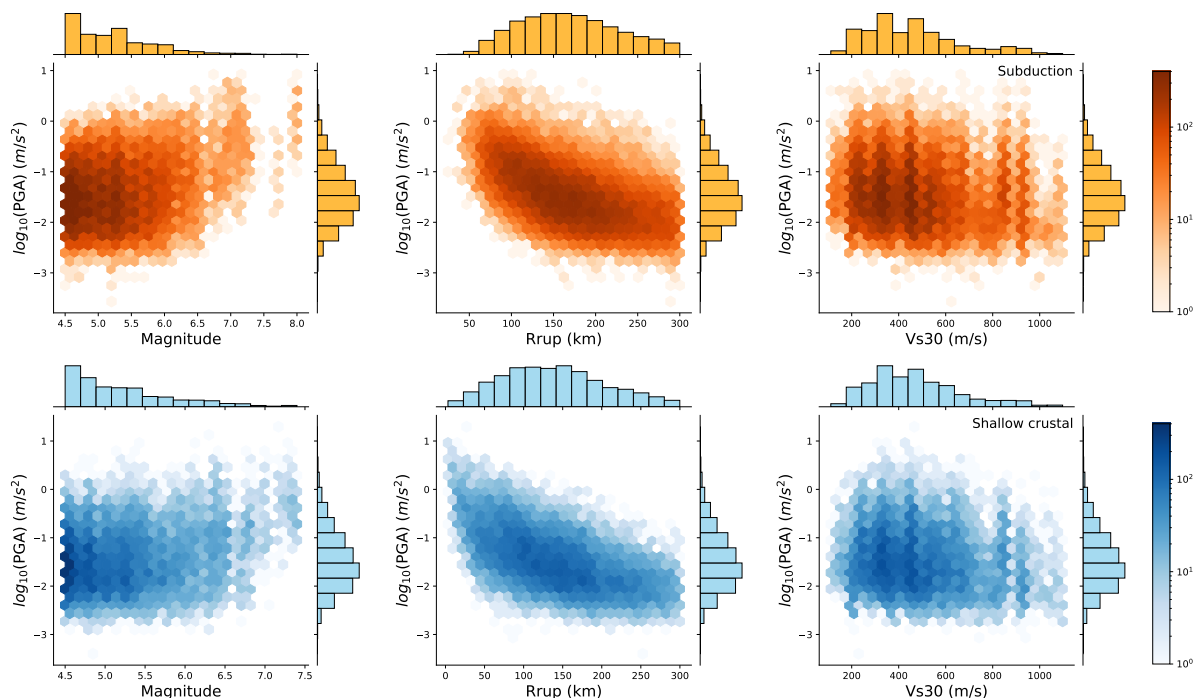


Figure 7: Distribution of earthquake magnitude, rupture distance, and V_{S30} versus $\log_{10}(\text{PGA})$ for the subduction (first row) and shallow crustal (second row) events.

where, $\text{cov}(\epsilon_{T_1}, \epsilon_{T_2})$ is the covariance between the two periods, and $\sigma_{\epsilon_{T_1}}$ and $\sigma_{\epsilon_{T_2}}$ are the standard deviations at T_1 and T_2 , respectively, as determined empirically from the synthetic ground motions. In this example, we see a stronger correlation between the $T=1.0$ s and $T=2.0$ s residuals ($\rho=0.78$) than the $T=1.0$ s and $T=0.2$ s residuals ($\rho=0.29$), which are further apart in log space. This observation is in agreement with Baker (2011), who found the correlation coefficient between these pairs to be 0.75 and 0.44, respectively, for shallow crustal events. This example suggests that cGM-GANO is capable of learning the intricate characteristics of ground motion databases, such as the RotD50 inter-period correlation, that can be important in the seismic response of multi-modal structures.

Next, as we did with the verification SCEC BBP dataset, we tested the capability of cGM-GANO to learn the magnitude and distance scaling in sparsely sampled regions of the training dataset. In Fig 14, we show scenarios of RotD50 scaling versus magnitude, distance, and V_{S30} generated by cGM-GANO. The cGM-GANO-generated ground motions generally follow the mean and aleatory variability of the observations. In particular, they are able to capture the non-linear distance scaling at periods $T = 0.1, 1.0, 10.0s$, and the magnitude and V_{S30} scaling at periods $T = 1.0s$.

4.1 Validation against empirical GMMs

Lastly, we performed a series of comparisons of the cGM-GANO generated ground motions, trained on the KiK-net data set, to selected published ground motion models (GMMs) described in Section Residual Analysis and Comparison to Empirical Ground Motion Models. Fig. 15 compares the PSA magnitude and distance scaling of the cGM-GANO generated ground motions for shallow crustal events with the NGA-West 2 GMMs. Overall, cGM-GANO magnitude and distance scaling show similar trends with the published models in terms of median ground motion and aleatory variability. The biggest difference is at short distances which as explained above is believed to be a result of sparse data to constrain the model over that distance range. Similar comparisons are made in Fig. 16 against the BA18 EAS GMM. Here, a systematic misfit is observed at $f < 1$ Hz, which is introduced by the misfit between BA18 and the training data set; cGM-GANO scaling is consistent with the training dataset. Otherwise, similar conclusions are drawn for the median magnitude and distance scaling. The underestimation of EAS aleatory variability by cGM-GANO compared to BA18 and the cause of the misfit between the BA18 and the data will be further investigated by the authors.

For the subduction events, PSA scaling is compared in Fig. 17. The synthetic ground motions have consistent scaling with BChydro both in terms of median ground motion and aleatory variability over the entire frequency range. The

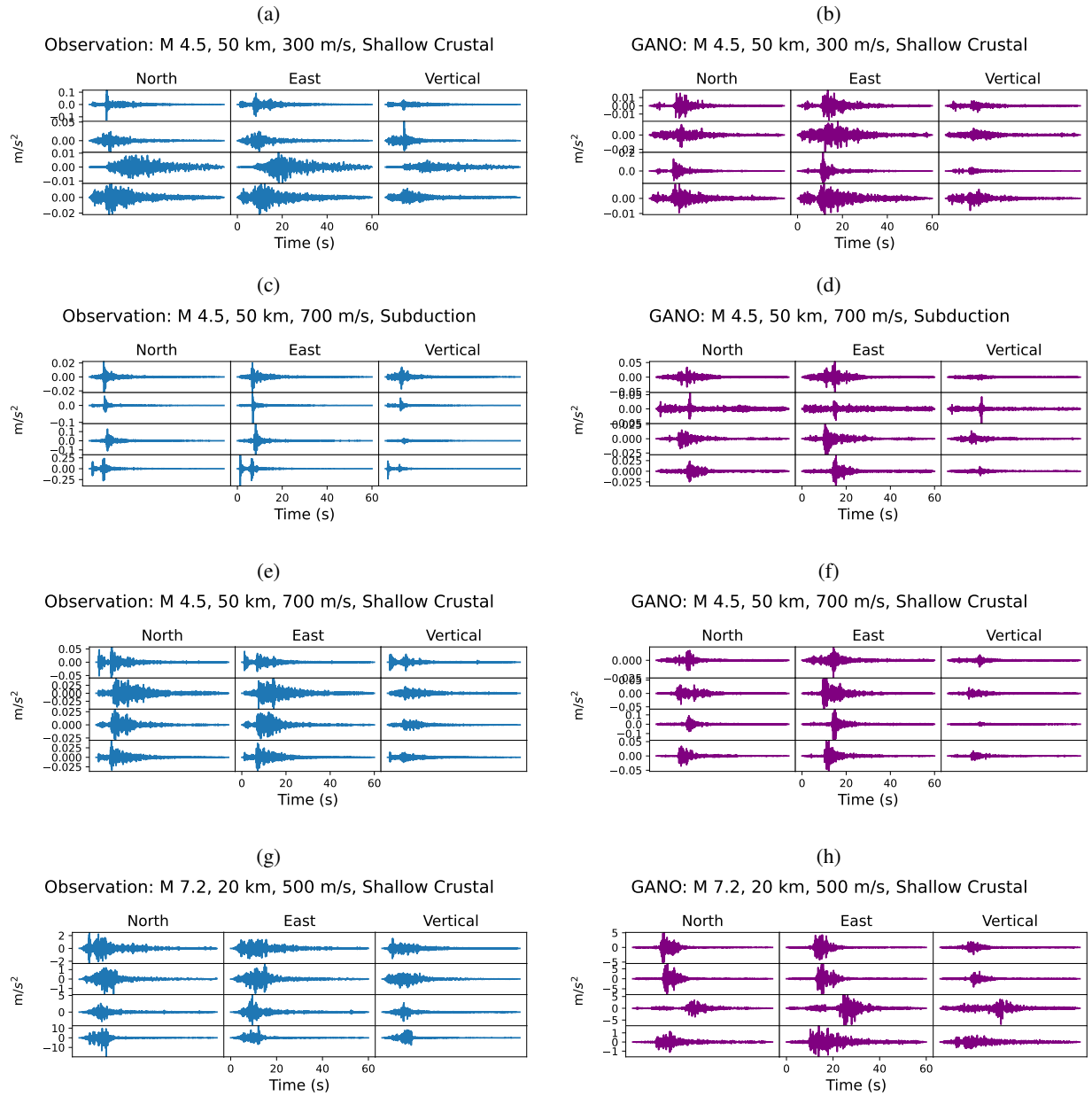


Figure 8: Accelerograms comparisons real and synthetically generated ground motions for cGM-GANO trained on the Kik-net dataset.

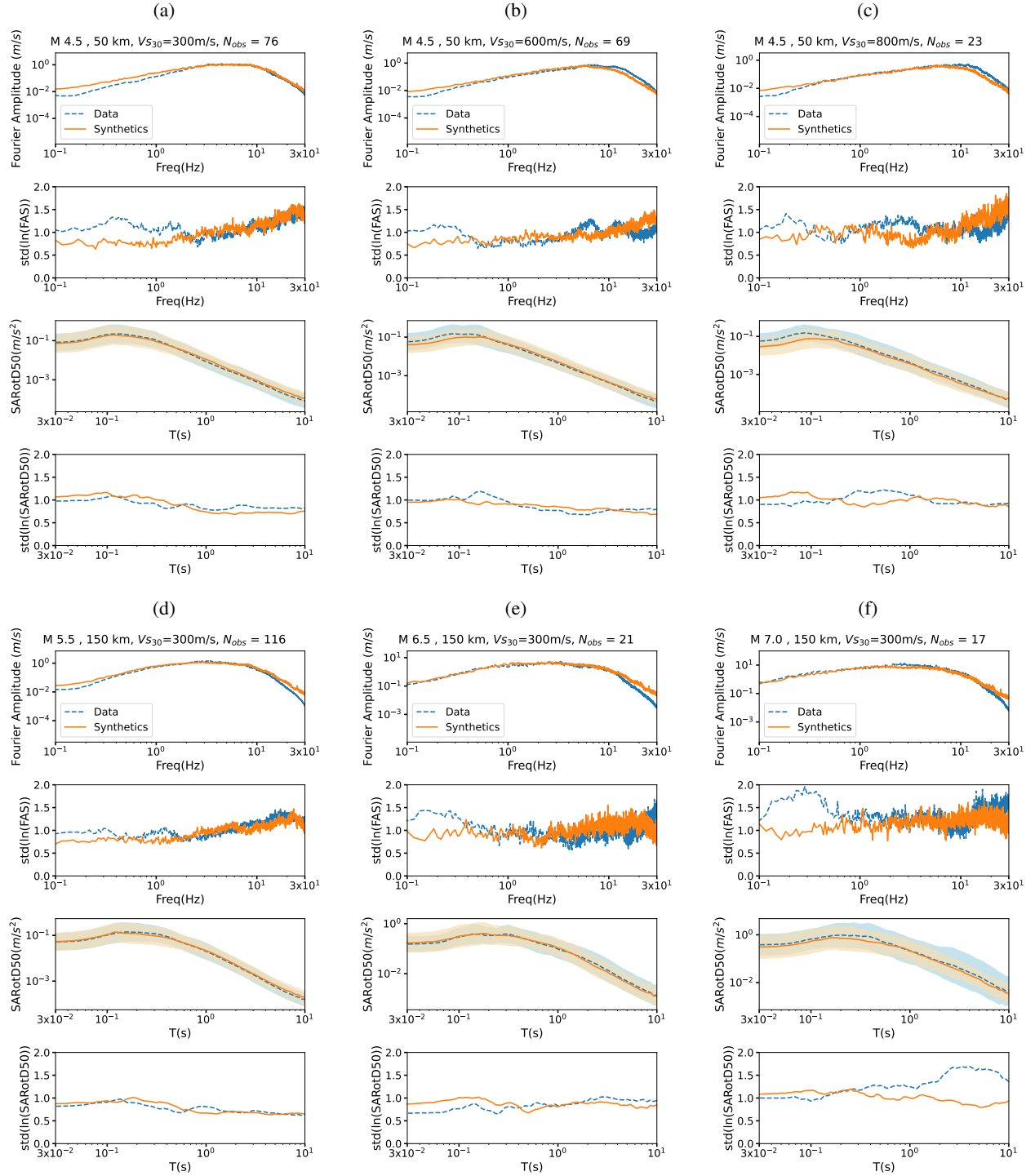


Figure 9: Scenario event comparisons for cGM-GANO trained on the kik-net dataset. Each sub-panel depicts the Fourier Amplitude Spectrum (FAS), aleatory standard deviation of FAS, Rotd50 Pseudo-spectral acceleration (PSA) spectrum, and aleatory standard deviation of Rotd50 PSA. The title of each plot corresponds to the midpoint of each bin, and N_{obs} is the number of observed records within each bin. The lines represent the mean in log space of the horizontal components of the synthetic (solid line) or kik-net (dashed line) data, while the shaded zone represents the 16th to 84th percentile range.

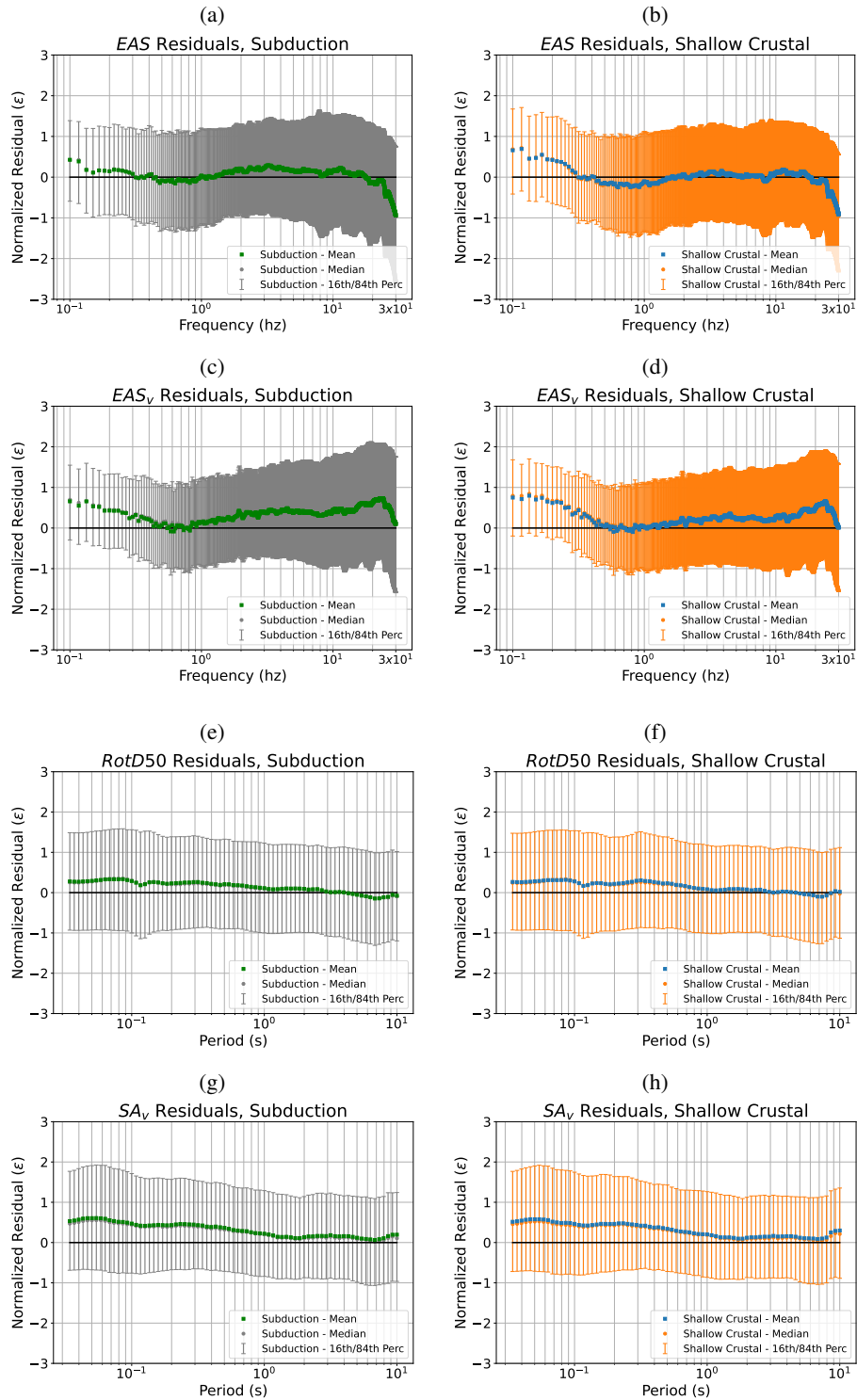


Figure 10: Residual plots of the kik-net trained model. Subfigures (a) and (b) show the horizontal EAS residuals for subduction and shallow crustal events, respectively. Subfigures (c) and (d) show the vertical EAS residuals for subduction and shallow crustal events, respectively. Subfigures (e) and (f) show the horizontal RotD50 PSA residuals for subduction and shallow crustal events, respectively. Subfigures (g) and (h) show the vertical PSA residuals for subduction and shallow crustal events, respectively.

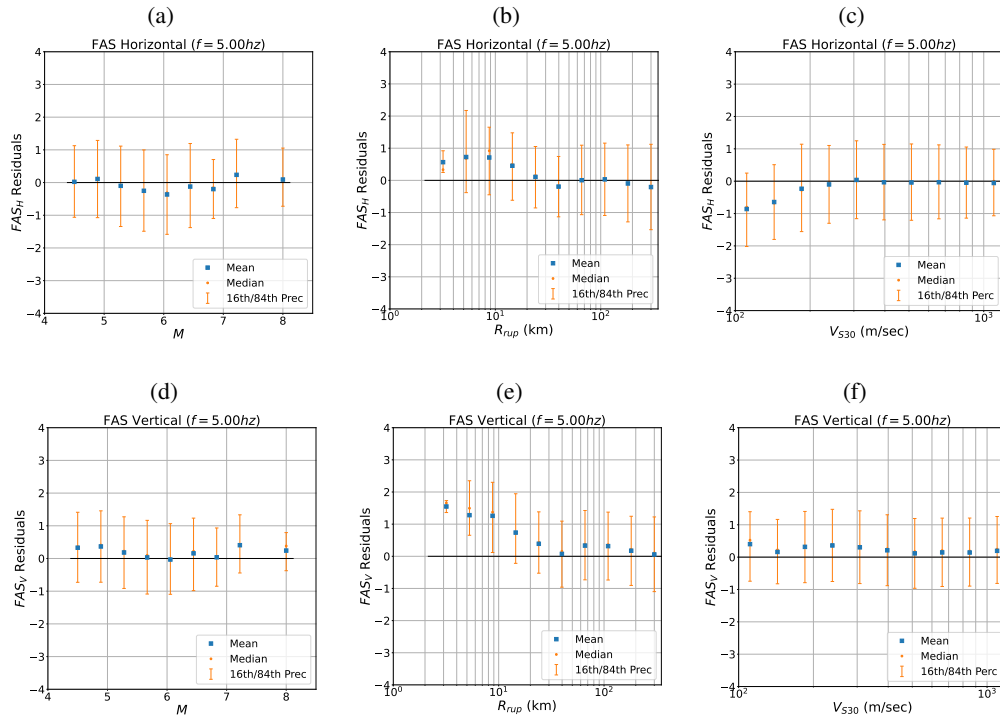


Figure 11: Comparison of horizontal and vertical FAS residuals for $f=5.0$ Hz against magnitude (subfigure (a) and (d), R_{rup} (subfigure (b) and (e)), and V_{S30} (subfigure (c) and (f))

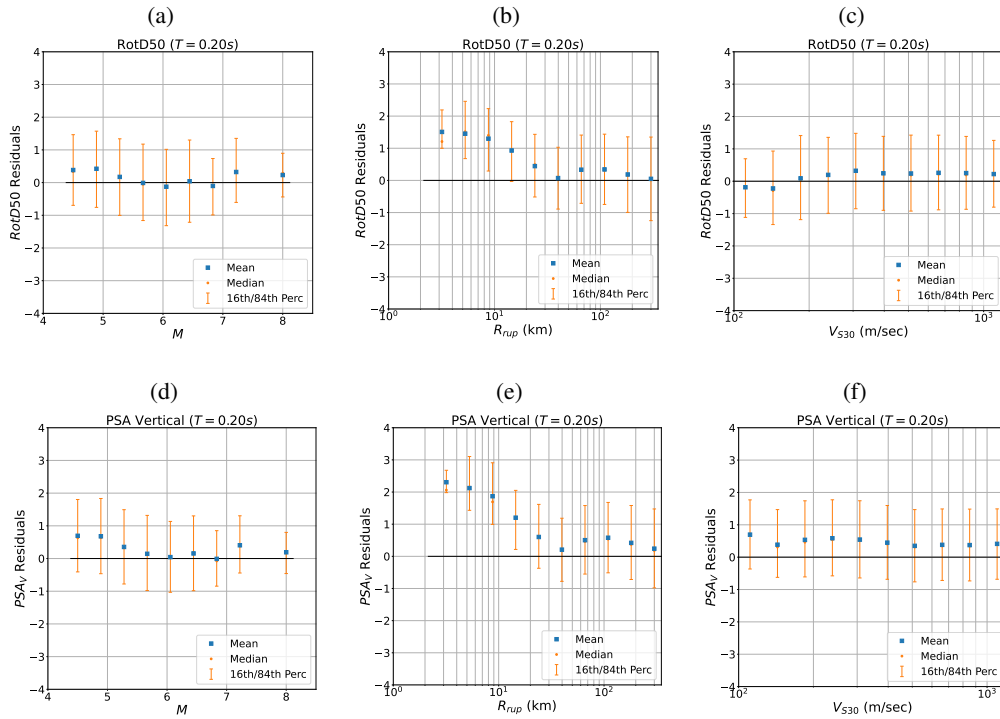


Figure 12: Comparison of horizontal and vertical PSA residuals for $T=0.2$ s ($f=5.0$ Hz) against magnitude (subfigure (a) and (d), R_{rup} (subfigure (b) and (e)), and V_{S30} (subfigure (c) and (f))

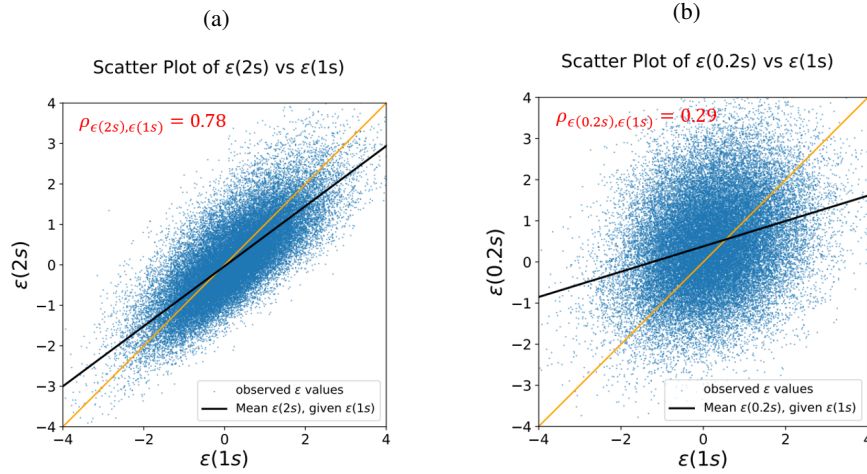


Figure 13: Inter-period correlation of horizontal PSA residuals. Between $T = 1$ s and $T = 2$ s in subfigure (a), and between $T = 1$ s and $T = 0.2$ s in subfigure (b).

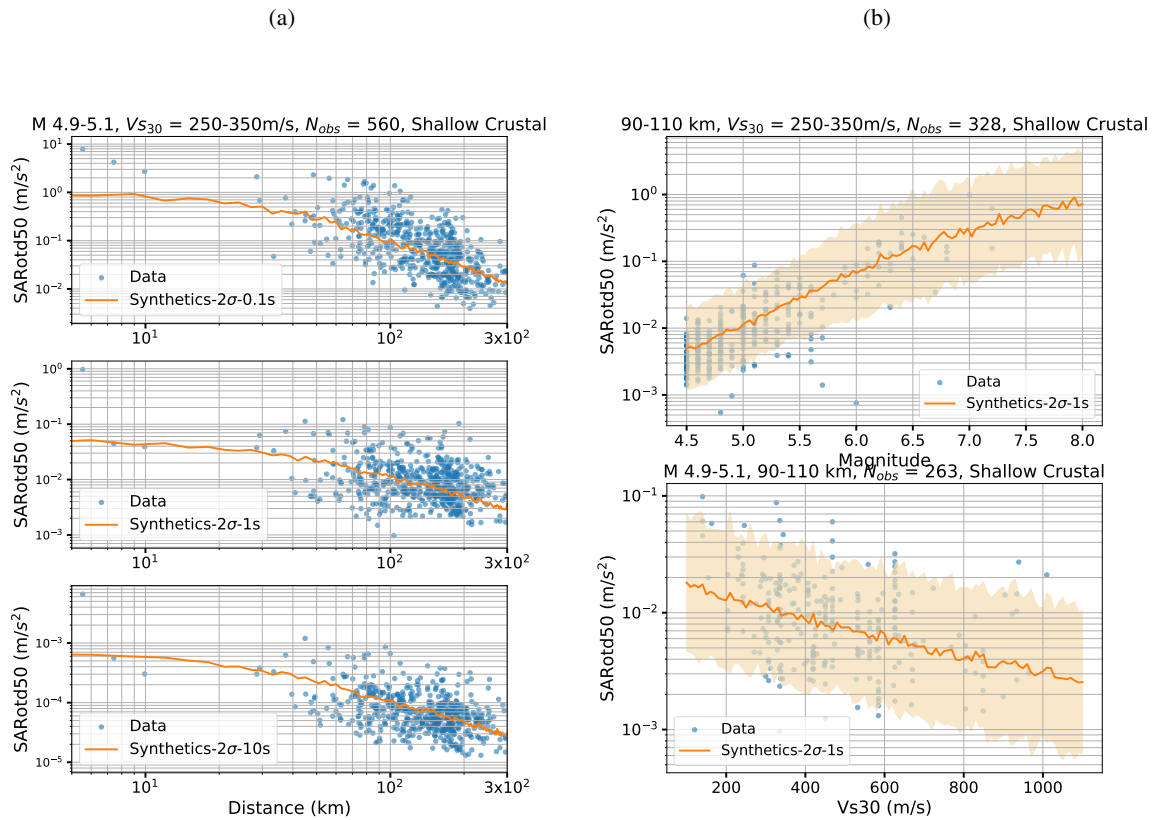


Figure 14: Comparison PSA distance, magnitude, and V_{S30} scaling of cmGM-GANO with Kik-net dataset. Left panels, from top to bottom, show the distance scaling for $T = 0.1$, 1.0 , and 10 s. Top right panel shows the magnitude scaling for $T = 1.0$ s. Bottom right panel shows the V_{S30} scaling for $T = 1.0$ s. Solid lines represent the mean scaling in log space. The shaded region shows the 2^{nd} to 98^{th} percentile of aleatory variability. Solid dots correspond to the Kik-net data.

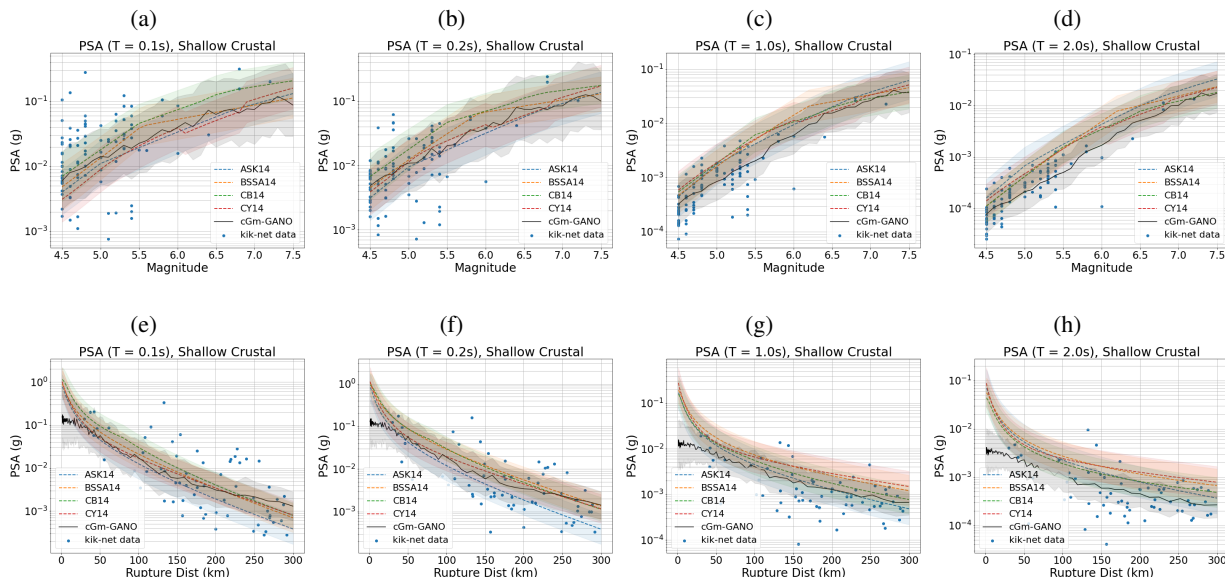


Figure 15: Comparison of cGM-GANO PSA scaling for shallow crustal events against the NGA-West2 GMMs. Top panel shows the magnitude comparison for $R_{rup} = 60$ km and $V_{s30} = 700$ m/s, at $T = 0.1, 0.2, 1, 2$ s ($f = 10, 5, 1, 0.5$ Hz), respectively. Bottom panel shows the distance comparison for $M = 6$ km and $V_{s30} = 700$ m/s, km, for the same frequencies. Solid lines represent the median scaling, the shaded region corresponds to the 16th to 84th percentile.

main misfit is observed at short distances. cGM-GANO is believed to have better performance for subduction events compared to shallow crustal due to the larger dataset size.

5 Summary and Discussion

We presented a data-driven model for conditional ground motion synthesis that can be used to generate 3-component ground motion time series covering a broadband range of frequencies. The model is based on the architecture of Neural Operators, a resolution-invariant generalization of Neural Networks. The ground motion synthesis is conditioned on moment magnitude (M), rupture distance (R_{rup}), time-average shear-wave velocity at the top 30m of the crust (V_{s30}), and tectonic environment or style of faulting (f_{type}).

Technical advancements of this work compared to previous efforts, including of the authors', are the use of Neural Operators and training of the model on velocity time series. Using Neural Operators guarantees both discretization-invariance of the model from the resolution of the training data set and universal approximation. We specifically employed the U-shaped Neural Operator (U-NO) architecture, which alleviates some issues associated with the memory requirements of fully connected Neural Operators. As well as, the training on velocity time series (as opposed to the target acceleration ground motions) also led to performance improvements due to the flatter Fourier spectral shape of the training signals.

The model was verified against a dataset of simulated ground motion time series from the SCEC BBP. The comparison of scenarios in terms of Fourier amplitude in the low-frequency regime $f < 1$ Hz ($T > 1$ sec) systematically showed the mean and standard deviation of the simulated and cGM-GANO-generated time series to be in agreement. At the same time, for higher frequencies, the cGM-GANO-generated time series of the same scenarios have systematically higher variability and a positive bias for reverse events. Our working hypothesis for the discontinuity that occurs at $f = 1$ Hz, the cross-over period between the low- and high-frequency methods in the BBP hybrid GP module, is that cGM-GANO cannot learn the stochastic high-frequency method, and resorts to carrying over the learned PDE solution of $f < 1$ Hz into the higher frequency range. The comparison of the response spectral ordinates showed a small constant positive bias across the period range for both styles of faulting. This bias is attributed to an unsuitable inter-period correlation of the synthetic ground motions that are influenced by the stochastic component of the training dataset; however, further investigation is needed.

The model was next trained and compared to a dataset curated and processed from observations recorded by the Japanese strong motion network KiK-net, which contains both shallow crustal and subduction events. Bias was observed in

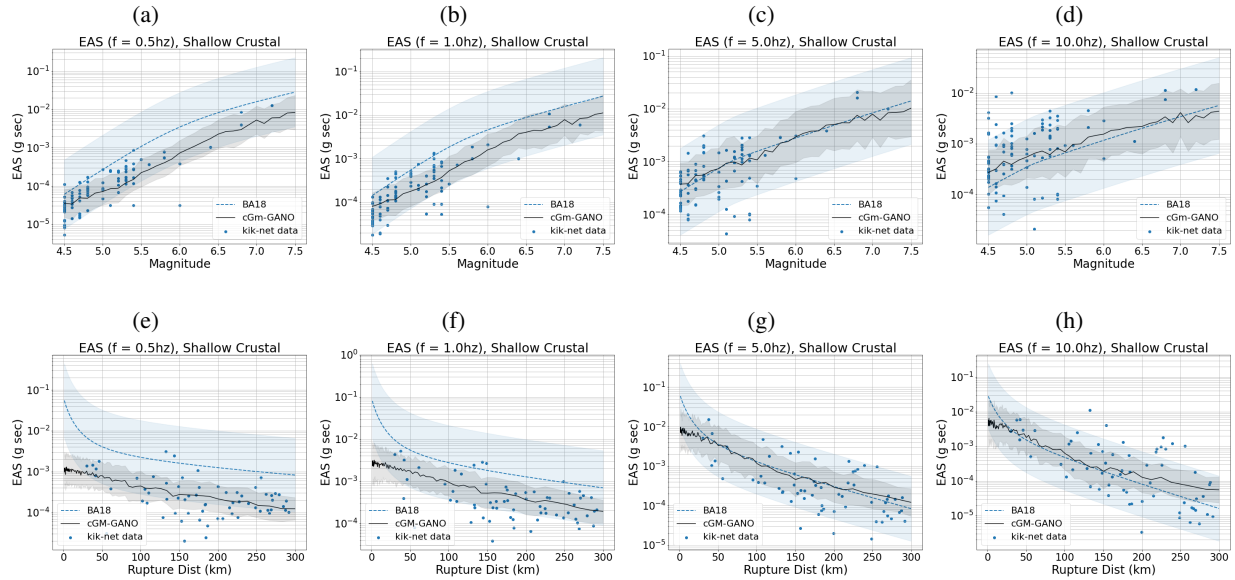


Figure 16: Comparison of cGM-GANO EAS scaling for shallow crustal events against the BA18 EAS GMMs. Top panel shows the magnitude comparison for $R_{rup} = 60$ km and $V_{s30} = 700$ m/s, at $f = 0.5, 1, 5,$ and 10 Hz, respectively. Bottom panel shows the distance comparison for $M = 6$ km and $V_{s30} = 700$ m/s, km, for the same frequencies. Solid lines represent the median scaling, the shaded region corresponds to the 16th to 84th percentile.

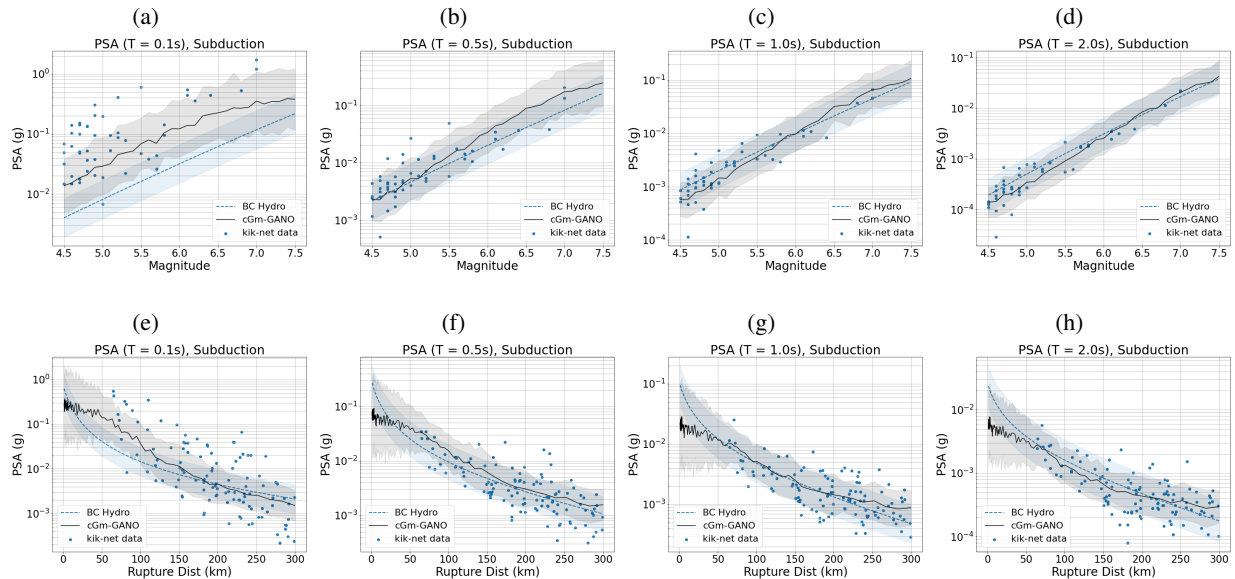


Figure 17: Comparison of cGM-GANO PSA scaling for subduction events against BC-Hydro GMM. Top panel shows the magnitude comparison for $R_{rup} = 60$ km and $V_{s30} = 700$ m/s, at $T = 0.1, 0.5, 1,$ and 2 s ($f = 10, 2, 1,$ and 0.5 Hz), respectively. Bottom panel shows the distance comparison for $M = 6$ km and $V_{s30} = 700$ m/s, km, for the same frequencies. Solid lines represent the median scaling, the shaded region corresponds to the 16th to 84th percentile.

the distance scaling of near field ground motions and V_{S30} scaling for soft soil sites, which we attributed to a lack of adequate training data in the corresponding regimes: in the first case, the training dataset contains less than 0.5% of ground motions recorded at stations with $R_{rup} \leq 20$ km; in the second case, the training dataset was larger but we hypothesize that cGM-GANO is also called to learn the scaling that includes nonlinear site response, and as such, requires an even larger amount of soft site data. This last hypothesis is being tested by the authors as part of a separate project.

Comparisons with traditional ground motion models (GMMs) led to similar conclusions: the cGM-GANO generated ground motions showed consistent median scaling with the GMMs for the corresponding tectonic environments. The largest misfit was observed at short distances due to the scarcity of training data, as mentioned above. A systematic misfit in EAS in the low-frequency regime ($f < 1\text{Hz}$) between cGM-GANO and BA18 is likely caused by the inconsistency of the available data and the GMM. The EAS variability, on the other hand, is underestimated across the entire frequency range. The source of the variability inconsistency between data, cGM-GANO, and GMMs is currently under investigation by the authors. The median scaling of PSA is better captured by cGM-GANO, except at short distances, and the aleatory variability is more accurately recovered, especially for subduction events, due to the availability of the data.

Ongoing work by the authors focuses on addressing the limitations of the model training and on expanding the overall framework. Until recently, strong motions recorded by the National Research Institute for Earth Science and Disaster Resilience (NIED) have been the only available open-access datasets that could be used in the training of cGM-GANO. As publicly available, larger and higher quality recorded datasets from regions such as California are slowly emerging, we plan to use them to improve the distance scaling over short distances and the V_{S30} scaling at soft soils of cGM-GANO, as well as to resolve the bias observed in the low-frequency range of the empirical dataset presented here. Further validations with traditional GMMs will also be performed, including duration and intensity of ground shaking intensity measures. For conditions not well constrained in the empirical data, we plan to employ additional techniques, such as reinforcement learning with physics-based simulations.

Framework enhancements that we are investigating include the effects of ground motion filtering and instrument direction, as well as the partitioning of the stochastic component into within and between event variability. More specifically, in its current architecture, cGM-GANO does not recognize the effect of filtering in recorded ground motions, and thus, any differences in the filtering of ground motions are mapped onto the stochastic component of cGM-GANO output. Similarly, the horizontal components are currently being provided in the North and South direction, irrespective of the fault’s azimuth, but, as past studies (e.g., Wald and Heaton, 1994; Archuleta, 1984) have demonstrated, radiation patterns and thus the fault’s azimuth can have a significant impact in the ground motion amplitude. Last, in this study’s framework, each ground motion realization is produced for a random event, which may be adequate for characterizing the seismic risk of individual structures, but it is not suitable for evaluating the seismic risk at a system’s level. These improvements are developed as part of several ongoing projects led by the authors, and the results thereof will be submitted for publication consideration in forthcoming manuscripts.

Data-driven models for ground motion synthesis may still be at the pilot stage, but with further refinements, they have the potential to bridge the gap between physics-based simulations and empirical models. Already in its current form, cGM-GANO can generate hundreds of site-specific realistic 3-component coherent ground motions with clear P-S arrivals and surface waves –currently only feasible with physics-based simulations– with the simplicity of empirical methods in less than a second. One should also consider this: data-driven generated ground motions can span a broad range of frequencies (up to 30 Hz in this study), all of which are learned from real recorded ground motion data. By contrast, physics-based simulations may have broken the computational barrier of high-frequency deterministic wave propagation with EXASCALE computing, but they will continue to lag behind the empirical ground motion models in the high-frequency regime until the propagation medium reaches the input resolution necessary for these frequencies to realistically propagate through and be modified appropriately by the heterogeneous, nonlinear shallow crust.

6 Data and Resources

KiK-net time histories can be downloaded through National Research Institute for Earth Science and Disaster Resilience <https://www.bosai.go.jp/e/index.html>, while the kik-net flatfile of the selected events is summarized in Bahrapouri et al. (2021) and can be downloaded through DesignSafe <https://www.designsafe-ci.org/data/browser/public>. The code for cGM-GANO is published on <https://github.com/yzshi5/GM-GANO>. The supplementary material contains a graphical example supporting the selection of velocity time series as our training data (Fig. S1); a realization of fault and station locations for the BBP simulations, depicting the sparsity of the recorded ground motions (Fig. S2); two scenarios of M7.0 events at 10km simulated using the BBP for reverse and strike-slip faults in the time and frequency domains, and their comparison to cGM-GANO generated ground motions for the

same conditional variables (Fig. S3); the inter-frequency correlation of the cGM-GANO ground motions for the model trained on BBP, clearly depicting the separation between the deterministic and stochastic regimes of the algorithm (Fig. S4); residual plots of the KiK-net trained model based on the validation (hold-off) dataset (Fig. S5); velocity time histories from observations and cGM-GANO generated ground motions using the model trained on the KiK-net data (Fig. S6); and displacement time histories from observations and cGM-GANO generated ground motions using the model trained on the KiK-net data (Fig. S7).

7 Declaration of Competing Interests

The authors declare no competing interests

8 Acknowledgments

We would like to thank Dr. Weiqiang Zhu and Dr. Mahdi Bahrampouri for their help during the curation and preprocessing of the KiK-net dataset. We would also like to thank Dr. Jian Shi and Dr. Robert W Graves for providing the BBP dataset. This material is based upon work supported in part by the U.S. Geological Survey under Grant No. G22AP00231. The views and conclusions contained in this document are those of the authors and should not be interpreted as representing the opinions or policies of the U.S. Geological Survey. Mention of trade names or commercial products does not constitute their endorsement by the U.S. Geological Survey. We would also like to thank Dr. Kim Olsen, an anonymous reviewer and associate editor, for the review and constructive comments that helped to improve the final article.

References

- Rameen Abdal, Peihao Zhu, Niloy Mitra, and Peter Wonka. StyleFlow: Attribute-conditioned Exploration of StyleGAN-Generated Images using Conditional Continuous Normalizing Flows, August 2020. URL <https://arxiv.org/abs/2008.02401v2>.
- Norman Abrahamson, Nicholas Gregor, and Kofi Addo. Bc hydro ground motion prediction equations for subduction earthquakes. *Earthquake Spectra*, 32(1):23–44, 2016.
- Norman A. Abrahamson, Walter J. Silva, and Ronnie Kamai. Summary of the ASK14 Ground Motion Relation for Active Crustal Regions. *Earthquake Spectra*, 30(3):1025–1055, August 2014. ISSN 8755-2930. doi: 10.1193/070913EQS198M. URL <https://doi.org/10.1193/070913EQS198M>.
- Ralph J Archuleta. A faulting model for the 1979 imperial valley earthquake. *Journal of Geophysical Research: Solid Earth*, 89(B6):4559–4585, 1984.
- Martin Arjovsky, Soumith Chintala, and Léon Bottou. Wasserstein Generative Adversarial Networks. In *Proceedings of the 34th International Conference on Machine Learning*, pages 214–223. PMLR, July 2017. URL <https://proceedings.mlr.press/v70/arjovsky17a.html>. ISSN: 2640-3498.
- Marco Baglio, Alessandro Cardoni, Gian Paolo Cimellaro, and Norman Abrahamson. Generating ground motions using the Fourier amplitude spectrum. *Earthquake Engineering & Structural Dynamics*, 52(15):4884–4899, 2023. ISSN 1096-9845. doi: 10.1002/eqe.3986. URL <https://onlinelibrary.wiley.com/doi/abs/10.1002/eqe.3986>. _eprint: <https://onlinelibrary.wiley.com/doi/pdf/10.1002/eqe.3986>.
- Mahdi Bahrampouri, Adrian Rodriguez-Marek, Shrey Shahi, and Haitham Dawood. An updated database for ground motion parameters for KiK-net records. *Earthquake Spectra*, 37(1):505–522, February 2021. ISSN 8755-2930. doi: 10.1177/8755293020952447. URL <https://doi.org/10.1177/8755293020952447>. Publisher: SAGE Publications Ltd STM.
- Jack Baker, Brendon Bradley, and Peter Stafford. *Seismic Hazard and Risk Analysis*. Cambridge University Press, Cambridge, 2021. ISBN 978-1-108-42505-6. doi: 10.1017/9781108425056. URL <https://www.cambridge.org/core/books/seismic-hazard-and-risk-analysis/177B4BA01FC2600AA53A22B27598A06C>.
- Jack W. Baker. Conditional Mean Spectrum: Tool for Ground-Motion Selection. *J. Struct. Eng.*, 137(3):322–331, March 2011. ISSN 0733-9445, 1943-541X. doi: 10.1061/(ASCE)ST.1943-541X.0000215. URL <http://ascelibrary.org/doi/10.1061/%28ASCE%29ST.1943-541X.0000215>.
- Jeff Bayless and Norman A. Abrahamson. An Empirical Model for the Interfrequency Correlation of Epsilon for Fourier Amplitude Spectra. *Bulletin of the Seismological Society of America*, 109(3):1058–1070, June 2019. ISSN 0037-1106, 1943-3573. doi: 10.1785/0120180238. URL <https://pubs.geoscienceworld.org/ssa/bssa/article/109/3/1058/570366/An-Empirical-Model-for-the-Interfrequency>.

- Avadhoot Bhosale, Robin Davis, and Pradip Sarkar. Vertical Irregularity of Buildings: Regularity Index versus Seismic Risk. *ASCE-ASME Journal of Risk and Uncertainty in Engineering Systems, Part A: Civil Engineering*, 3, January 2017. doi: 10.1061/AJRUAA6.0000900.
- D. M. Boore. Simulation of Ground Motion Using the Stochastic Method. *Pure appl. geophys.*, 160(3):635–676, March 2003. ISSN 1420-9136. doi: 10.1007/PL00012553. URL <https://doi.org/10.1007/PL00012553>.
- D. M. Boore. Orientation-Independent Measures of Ground Motion. *Bulletin of the Seismological Society of America*, 96(4A):1502–1511, August 2006. ISSN 0037-1106. doi: 10.1785/0120050209. URL <https://pubs.geoscienceworld.org/bssa/article/96/4A/1502-1511/146724>.
- D. M. Boore. Orientation-Independent, Nongeometric-Mean Measures of Seismic Intensity from Two Horizontal Components of Motion. *Bulletin of the Seismological Society of America*, 100(4):1830–1835, August 2010. ISSN 0037-1106. doi: 10.1785/0120090400. URL <https://pubs.geoscienceworld.org/bssa/article/100/4/1830-1835/349553>.
- David M. Boore. Stochastic simulation of high-frequency ground motions based on seismological models of the radiated spectra. *Bulletin of the Seismological Society of America*, 73(6A):1865–1894, December 1983. ISSN 0037-1106. doi: 10.1785/BSSA07306A1865. URL <https://doi.org/10.1785/BSSA07306A1865>.
- L. S. Burks and J. W. Baker. Validation of Ground-Motion Simulations through Simple Proxies for the Response of Engineered Systems. *Bulletin of the Seismological Society of America*, 104(4):1930–1946, August 2014. ISSN 0037-1106. doi: 10.1785/0120130276. URL <https://pubs.geoscienceworld.org/bssa/article/104/4/1930-1946/325580>.
- Mathieu Causse, Fabrice Cotton, Cécile Cornou, and Pierre-Yves Bard. Calibrating Median and Uncertainty Estimates for a Practical Use of Empirical Green’s Functions Technique. *Bulletin of the Seismological Society of America*, 98(1):344–353, February 2008. ISSN 0037-1106. doi: 10.1785/0120070075. URL <https://doi.org/10.1785/0120070075>.
- Mayssa Dabaghi and Armen Der Kiureghian. Stochastic model for simulation of near-fault ground motions. *Earthquake Engineering & Structural Dynamics*, 46(6):963–984, 2017. ISSN 1096-9845. doi: 10.1002/eqe.2839. URL <https://onlinelibrary.wiley.com/doi/abs/10.1002/eqe.2839>. _eprint: <https://onlinelibrary.wiley.com/doi/pdf/10.1002/eqe.2839>.
- John Douglas and Hideo Aochi. A Survey of Techniques for Predicting Earthquake Ground Motions for Engineering Purposes. *Surv Geophys*, 29(3):187, October 2008. ISSN 1573-0956. doi: 10.1007/s10712-008-9046-y. URL <https://doi.org/10.1007/s10712-008-9046-y>.
- Reza DD Esfahani, Fabrice Cotton, Matthias Ohrnberger, and Frank Scherbaum. Tfcgan: Nonstationary ground-motion simulation in the time–frequency domain using conditional generative adversarial network (cgan) and phase retrieval methods. *Bulletin of the Seismological Society of America*, 113(1):453–467, 2023.
- Manuel A. Florez, Michaelangelo Caporale, Pakpoom Buabthong, Zachary E. Ross, Domniki Asimaki, and Men-Andrin Meier. Data-Driven Synthesis of Broadband Earthquake Ground Motions Using Artificial Intelligence. *Bulletin of the Seismological Society of America*, 112(4):1979–1996, August 2022. ISSN 0037-1106, 1943-3573. doi: 10.1785/0120210264. URL <https://pubs.geoscienceworld.org/bssa/article/112/4/1979/613199/Data-Driven-Synthesis-of-Broadband-Earthquake>.
- Arthur Frankel. A Constant Stress-Drop Model for Producing Broadband Synthetic Seismograms: Comparison with the Next Generation Attenuation Relations. *Bulletin of the Seismological Society of America*, 99(2A):664–680, April 2009. ISSN 0037-1106. doi: 10.1785/0120080079. URL <https://doi.org/10.1785/0120080079>.
- David John Gagne, Hannah M Christensen, Aneesh C Subramanian, and Adam H Monahan. Machine learning for stochastic parameterization: Generative adversarial networks in the lorenz’96 model. *Journal of Advances in Modeling Earth Systems*, 12(3):e2019MS001896, 2020.
- Filippo Gatti and Didier Clouteau. Towards blending physics-based numerical simulations and seismic databases using generative adversarial network. *Computer Methods in Applied Mechanics and Engineering*, 372:113421, 2020.
- Ian Goodfellow, Jean Pouget-Abadie, Mehdi Mirza, Bing Xu, David Warde-Farley, Sherjil Ozair, Aaron Courville, and Yoshua Bengio. Generative adversarial nets. *Advances in neural information processing systems*, 27, 2014.
- Ian Goodfellow, Yoshua Bengio, and Aaron Courville. *Deep Learning*. MIT Press, November 2016. ISBN 978-0-262-33737-3. Google-Books-ID: omivDQAAQBAJ.
- Christine A. Goulet, Jennie Watson-Lamprey, Jack Baker, Curt Haselton, and Nico Luco. Assessment of Ground Motion Selection and Modification (GMSM) Methods for Non-Linear Dynamic Analyses of Structures. In *Geotechnical Earthquake Engineering and Soil Dynamics IV*, pages 1–10, Sacramento, California, United States, May 2008.

- American Society of Civil Engineers. ISBN 978-0-7844-0975-6. doi: 10.1061/40975(318)3. URL <http://ascelibrary.org/doi/10.1061/40975%28318%293>.
- Robert Graves and Arben Pitarka. Refinements to the graves and pitarka (2010) broadband ground-motion simulation method. *Seismological Research Letters*, 86(1):75–80, 2015.
- Robert W. Graves and Arben Pitarka. Broadband Ground-Motion Simulation Using a Hybrid Approach. *Bulletin of the Seismological Society of America*, 100(5A):2095–2123, October 2010. ISSN 0037-1106. doi: 10.1785/0120100057. URL <https://doi.org/10.1785/0120100057>.
- Thomas C. Hanks and Robin K. McGuire. The character of high-frequency strong ground motion. *Bulletin of the Seismological Society of America*, 71(6):2071–2095, December 1981. ISSN 0037-1106. doi: 10.1785/BSSA0710062071. URL <https://doi.org/10.1785/BSSA0710062071>.
- Evangelos I. Katsanos, Anastasios G. Sextos, and George D. Manolis. Selection of earthquake ground motion records: A state-of-the-art review from a structural engineering perspective. *Soil Dynamics and Earthquake Engineering*, 30(4):157–169, April 2010. ISSN 0267-7261. doi: 10.1016/j.soildyn.2009.10.005. URL <https://www.sciencedirect.com/science/article/pii/S0267726109001602>.
- Qingkai Kong, Daniel T Trugman, Zachary E Ross, Michael J Bianco, Brendan J Meade, and Peter Gerstoft. Machine learning in seismology: Turning data into insights. *Seismological Research Letters*, 90(1):3–14, 2019.
- Katsuaki Konno and Tatsuo Ohmachi. Ground-motion characteristics estimated from spectral ratio between horizontal and vertical components of microtremor. *Bulletin of the Seismological Society of America*, 88(1):228–241, 1998.
- Albert Kottke. arkottke/pyrotd v0.5.4, July 2018. URL <https://zenodo.org/record/1322849>.
- Albert R Kottke, Norman A Abrahamson, David M Boore, Yousef Bozorgnia, Christine A Goulet, Justin Hollenback, Tadahiro Kishida, Olga-Joan Ktenidou, Ellen M Rathje, Walter J Silva, et al. Selection of random vibration theory procedures for the nga-east project and ground-motion modeling. *Earthquake Spectra*, 37(1_suppl):1420–1439, 2021.
- Nikola Kovachki, Zongyi Li, Burigede Liu, Kamyar Azizzadenesheli, Kaushik Bhattacharya, Andrew Stuart, and Anima Anandkumar. Neural Operator: Learning Maps Between Function Spaces, December 2021. URL <http://arxiv.org/abs/2108.08481>. arXiv:2108.08481 [cs, math].
- Nikola Kovachki, Zongyi Li, Burigede Liu, Kamyar Azizzadenesheli, Kaushik Bhattacharya, Andrew Stuart, and Anima Anandkumar. Neural operator: Learning maps between function spaces with applications to pdes. *Journal of Machine Learning Research*, 24(89):1–97, 2023.
- Yuanming Li and Bonhwa ;Shou. Zhang;Jae-Kwang. Ahn ;Hanseok. Ko Ku. Seismic data augmentation based on conditional generative adversarial networks. *Sensors*, 20(23):6850, 2020.
- Zongyi Li, Nikola Kovachki, Kamyar Azizzadenesheli, Burigede Liu, Kaushik Bhattacharya, Andrew Stuart, and Anima Anandkumar. Neural Operator: Graph Kernel Network for Partial Differential Equations, March 2020. URL <http://arxiv.org/abs/2003.03485>. arXiv:2003.03485 [cs, math, stat].
- Zongyi Li, Nikola Kovachki, Kamyar Azizzadenesheli, Burigede Liu, Kaushik Bhattacharya, Andrew Stuart, and Anima Anandkumar. Fourier Neural Operator for Parametric Partial Differential Equations, May 2021. URL <http://arxiv.org/abs/2010.08895>. arXiv:2010.08895 [cs, math].
- Nicolas Luco and Paolo Bazzurro. Does amplitude scaling of ground motion records result in biased nonlinear structural drift responses? *Earthquake Engineering & Structural Dynamics*, 36(13):1813–1835, 2007. ISSN 1096-9845. doi: 10.1002/eqe.695. URL <https://onlinelibrary.wiley.com/doi/abs/10.1002/eqe.695>. eprint: <https://onlinelibrary.wiley.com/doi/pdf/10.1002/eqe.695>.
- Philip J. Maechling, Fabio Silva, Scott Callaghan, and Thomas H. Jordan. SCEC Broadband Platform: System Architecture and Software Implementation. *Seismological Research Letters*, 86(1):27–38, December 2014. ISSN 0895-0695. doi: 10.1785/0220140125. URL <https://doi.org/10.1785/0220140125>.
- Giuseppe Carlo Marano, Marco Martino Rosso, Angelo Aloisio, and Giansalvo Cirrincione. Generative adversarial networks review in earthquake-related engineering fields. *Bulletin of Earthquake Engineering*, pages 1–52, 2023.
- Mehrshad Matinfar, Naser Khaji, and Goodarz Ahmadi. Deep convolutional generative adversarial networks for the generation of numerous artificial spectrum-compatible earthquake accelerograms using a limited number of ground motion records. *Computer-Aided Civil and Infrastructure Engineering*, 38(2):225–240, 2023.
- David McCallen, Anders Petersson, Arthur Rodgers, Arben Pitarka, Mamun Miah, Floriana Petrone, Bjorn Sjogreen, Norman Abrahamson, and Houjun Tang. EQSIM—A multidisciplinary framework for fault-to-structure earthquake simulations on exascale computers part I: Computational models and workflow. *Earthquake Spectra*, 37(2):707–735, May 2021. ISSN 8755-2930. doi: 10.1177/8755293020970982. URL <https://doi.org/10.1177/8755293020970982>. Publisher: SAGE Publications Ltd STM.

- Farzad Naeim and Marshall Lew. On the Use of Design Spectrum Compatible Time Histories. *Earthquake Spectra*, 11(1):111–127, February 1995. ISSN 8755-2930. doi: 10.1193/1.1585805. URL <https://doi.org/10.1193/1.1585805>. Publisher: SAGE Publications Ltd STM.
- NIED. NIED K-NET, KiK-net, March 2019. URL https://nied-ir.bosai.go.jp/?action=pages_view_main&active_action=repository_view_main_item_detail&item_id=2146&item_no=1&page_id=13&block_id=245.
- Roberto Paolucci, Chiara Smerzini, and Manuela Vanini. BB-SPEEDset: A Validated Dataset of Broadband Near-Source Earthquake Ground Motions from 3D Physics-Based Numerical Simulations. *Bulletin of the Seismological Society of America*, 111(5):2527–2545, July 2021. ISSN 0037-1106. doi: 10.1785/0120210089. URL <https://doi.org/10.1785/0120210089>.
- Jaideep Pathak, Shashank Subramanian, Peter Harrington, Sanjeev Raja, Ashesh Chattopadhyay, Morteza Mardani, Thorsten Kurth, David Hall, Zongyi Li, Kamyar Azizzadenesheli, Pedram Hassanzadeh, Karthik Kashinath, and Animeshree Anandkumar. FourCastNet: A Global Data-driven High-resolution Weather Model using Adaptive Fourier Neural Operators, February 2022. URL <http://arxiv.org/abs/2202.11214>. arXiv:2202.11214 [physics].
- Arben Pitarka, Hong Kie Thio, Paul Somerville, and Luis Fabian Bonilla. Broadband Ground-Motion Simulation of an Intraslab Earthquake and Nonlinear Site Response: 2010 Ferndale, California, Earthquake Case Study. *Seismological Research Letters*, 84(5):785–795, September 2013. ISSN 0895-0695. doi: 10.1785/0220130031. URL <https://doi.org/10.1785/0220130031>.
- Manuel A.; Anima Anandkumar; Zachary E Ross ;Azizzadenesheli Kamyar Rahman, Md Ashiqur; Florez. Generative adversarial neural operators. *Transactions on Machine Learning Research*, 2022a. ISSN 2835-8856. URL <https://openreview.net/forum?id=X1VzbBU6xZ>.
- Zach E.; Kamyar Azizzadenesheli Rahman, Md Ashiqur; Ross. U-NO: U-shaped Neural Operators. *arXiv:2204.11127 [cs]*, page 12, April 2022b. arXiv: 2204.11127.
- Sanaz Rezaeian and Armen Der Kiureghian. Simulation of orthogonal horizontal ground motion components for specified earthquake and site characteristics. *Earthquake Engineering & Structural Dynamics*, 41(2):335–353, 2012. ISSN 1096-9845. doi: 10.1002/eqe.1132. URL <https://onlinelibrary.wiley.com/doi/abs/10.1002/eqe.1132>. eprint: <https://onlinelibrary.wiley.com/doi/pdf/10.1002/eqe.1132>.
- Arthur J Rodgers, Arben Pitarka, Ramesh Pankajakshan, Bjorn Sjögreen, and N Anders Petersson. Regional-scale 3d ground-motion simulations of mw 7 earthquakes on the hayward fault, northern california resolving frequencies 0–10 hz and including site-response corrections. *Bulletin of the Seismological Society of America*, 110(6):2862–2881, 2020.
- Olaf Ronneberger, Philipp Fischer, and Thomas Brox. U-Net: Convolutional Networks for Biomedical Image Segmentation, May 2015. URL <http://arxiv.org/abs/1505.04597>. arXiv:1505.04597 [cs].
- Fabio Sabetta, Antonio Pugliese, Gabriele Fiorentino, Giovanni Lanzano, and Lucia Luzi. Simulation of non-stationary stochastic ground motions based on recent Italian earthquakes. *Bulletin of Earthquake Engineering*, 19(9):3287–3315, April 2021. ISSN 1570-761X. doi: 10.1007/s10518-021-01077-1.
- Jian Shi. *Improving Site Response Analysis for Earthquake Ground Motion Modeling*. PhD thesis, California Institute of Technology, 2019.
- Peter J. Stafford. Interfrequency Correlations among Fourier Spectral Ordinates and Implications for Stochastic Ground-Motion Simulation. *Bulletin of the Seismological Society of America*, 107(6):2774–2791, December 2017. ISSN 0037-1106, 1943-3573. doi: 10.1785/0120170081. URL <https://pubs.geoscienceworld.org/bssa/article-lookup?doi=10.1785/0120170081>.
- Behrooz Tavakoli and Shahram Pezeshk. Empirical-Stochastic Ground-Motion Prediction for Eastern North America. *Bulletin of the Seismological Society of America*, 95(6):2283–2296, December 2005. ISSN 0037-1106. doi: 10.1785/0120050030. URL <https://doi.org/10.1785/0120050030>.
- Sara Touhami, Filippo Gatti, Fernando Lopez-Caballero, Régis Cottureau, Lúcio de Abreu Corrêa, Ludovic Aubry, and Didier Clouteau. SEM3D: A 3D High-Fidelity Numerical Earthquake Simulator for Broadband (0–10 Hz) Seismic Response Prediction at a Regional Scale. *Geosciences*, 12(3):112, March 2022. ISSN 2076-3263. doi: 10.3390/geosciences12030112. URL <https://www.mdpi.com/2076-3263/12/3/112>. Number: 3 Publisher: Multidisciplinary Digital Publishing Institute.
- David J Wald and Thomas H Heaton. Spatial and temporal distribution of slip for the 1992 landers, california, earthquake. *Bulletin of the Seismological Society of America*, 84(3):668–691, 1994.
- Daniel; Youzuo. Lin Wang, Tiantong, Trugman. Seismogen: Seismic waveform synthesis using gan with application to seismic data augmentation. *Journal of Geophysical Research: Solid Earth*, 126(4):e2020JB020077, 2021a.

- Teng; Brian. Lovell Wang, Tianren; Zhang. Faces à la Carte: Text-to-Face Generation via Attribute Disentanglement. In *2021 IEEE Winter Conference on Applications of Computer Vision (WACV)*, pages 3379–3387, Waikoloa, HI, USA, January 2021b. IEEE. ISBN 978-1-66540-477-8. doi: 10.1109/WACV48630.2021.00342. URL <https://ieeexplore.ieee.org/document/9423291/>.
- Tiantong Wang, Zhongping Zhang, and Youzuo Li. Earthquakegen: Earthquake generator using generative adversarial networks. In *SEG International Exposition and Annual Meeting*, page D043S119R004. SEG, 2019.
- Gege Wen, Zongyi Li, Kamyar Azizzadenesheli, Anima Anandkumar, and Sally M. Benson. U-FNO – An enhanced Fourier neural operator-based deep-learning model for multiphase flow, May 2022. URL <http://arxiv.org/abs/2109.03697>. arXiv:2109.03697 [physics].
- Yuxin Wu and Kaiming He. Group Normalization. pages 3–19, 2018. URL https://openaccess.thecvf.com/content_ECCV_2018/html/Yuxin_Wu_Group_Normalization_ECCV_2018_paper.html.
- Yan Yang, Angela F. Gao, Jorge C. Castellanos, Zachary E. Ross, Kamyar Azizzadenesheli, and Robert W. Clayton. Seismic Wave Propagation and Inversion with Neural Operators. *The Seismic Record*, 1(3):126–134, November 2021. ISSN 2694-4006. doi: 10.1785/0320210026. URL <https://doi.org/10.1785/0320210026>.

Supplementary Material to Broadband Ground Motion Synthesis via Generative Adversarial Neural Operators: Development and Validation

Shi Y., Lavrentiadis G., Asimaki D., Ross Z.E., and Azizzadenesheli K.

February 16, 2024

As an illustrative example, Fig S1. compares the time history and Fourier Amplitude Spectrum acceleration, velocity, and displacement of a M_w 6.9, $R_{rup} = 23\text{km}$ event recorded at station ISKH02 of the Kik-Net strong motion network with $V_{s30} = 721\text{m/s}$. In the figure, the acceleration time series are rich in high frequencies and attain constant Fourier spectral content at frequencies larger than $\sim 5\text{Hz}$. The opposite is true for displacement time series, their energy content decays for frequencies higher than 0.1Hz . Spanning a much broader frequency range of spectral amplitudes from ~ 0.1 to 10Hz , the velocity time series provided the optimal balance of input frequency content to train cGM-GANO in the broadband frequency range $0.1 \sim 30\text{Hz}$.

Fig S2 shows the fault location (indicated by the black line) and the corresponding station positions (depicted as red dots) used in the BBP simulation. The yellow star on the fault represents the hypocenter.

Fig S3 compares acceleration time history and Fourier amplitude spectrum of BBP and cGM-GANO generated ground motions for both strike-slip and reverse scenarios under $M_w = 7.0$, $R_{rup} = 10\text{ km}$. In this figure, cGM-GANO captures the envelope of the BBP waveforms in the time domain. In the frequency domain.

Fig S4 presents the inter-frequency correlation of the cGM-GANO synthetically generated ground motions based on the BBP dataset.

Fig S5 shows the residual results of Fig 10 using only the validation Kik-Net dataset; that is, the subset not included in the training of cGM-GANO. The negligible differences between Fig 10 and S5 indicate no overfitting on the training dataset.

Fig S6 and S7 compare the velocity and displacement time histories between data and synthetic ground motions from cGM-GANO for the same scenarios shown in Figure 8.

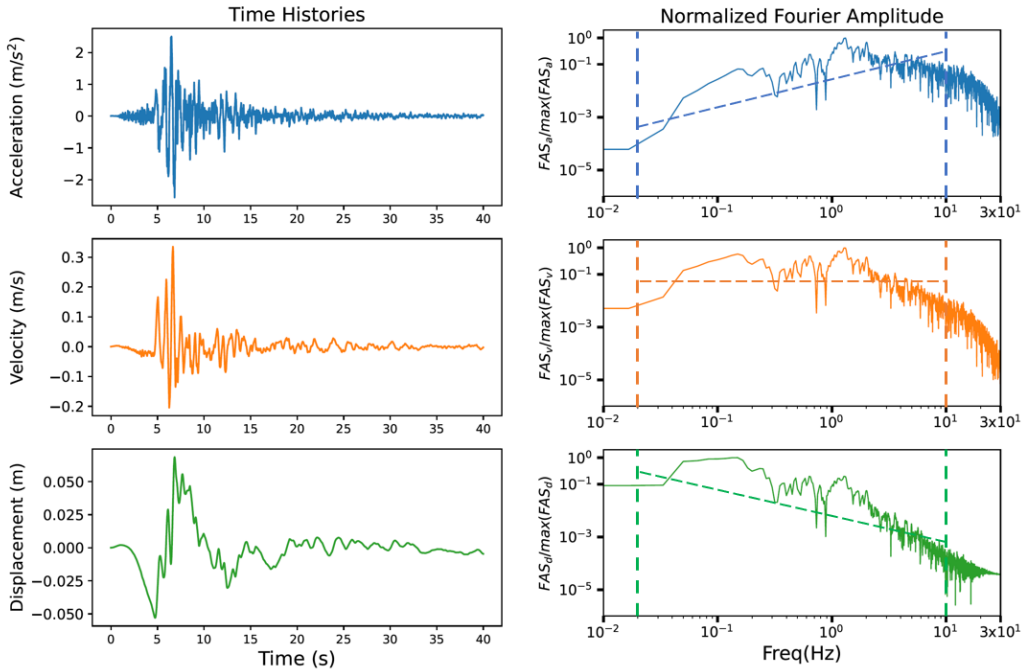


Figure 1: Example of frequency content shift between acceleration, velocity, and displacement time series, depicted in the time and frequency domain. Example time series corresponds to event id ISKH020703250942 with $M_w = 6.9$ and $R_{rup} = 23km$ from the Kik-net dataset. The left-hand panels show the acceleration, velocity, and displacement time series from top to bottom, while the right-hand panels show the corresponding normalized frequency amplitude spectra. Each spectrum is normalized by its maximum amplitude. The dash lines show the FAS trend in 0.02Hz ~ 10Hz frequency range.

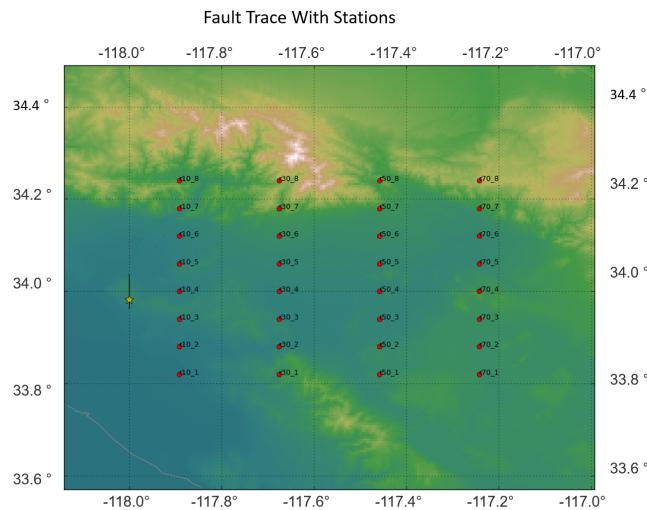


Figure 2: An example of the location of the fault (black line) and stations (red dots) used in BBP simulation.

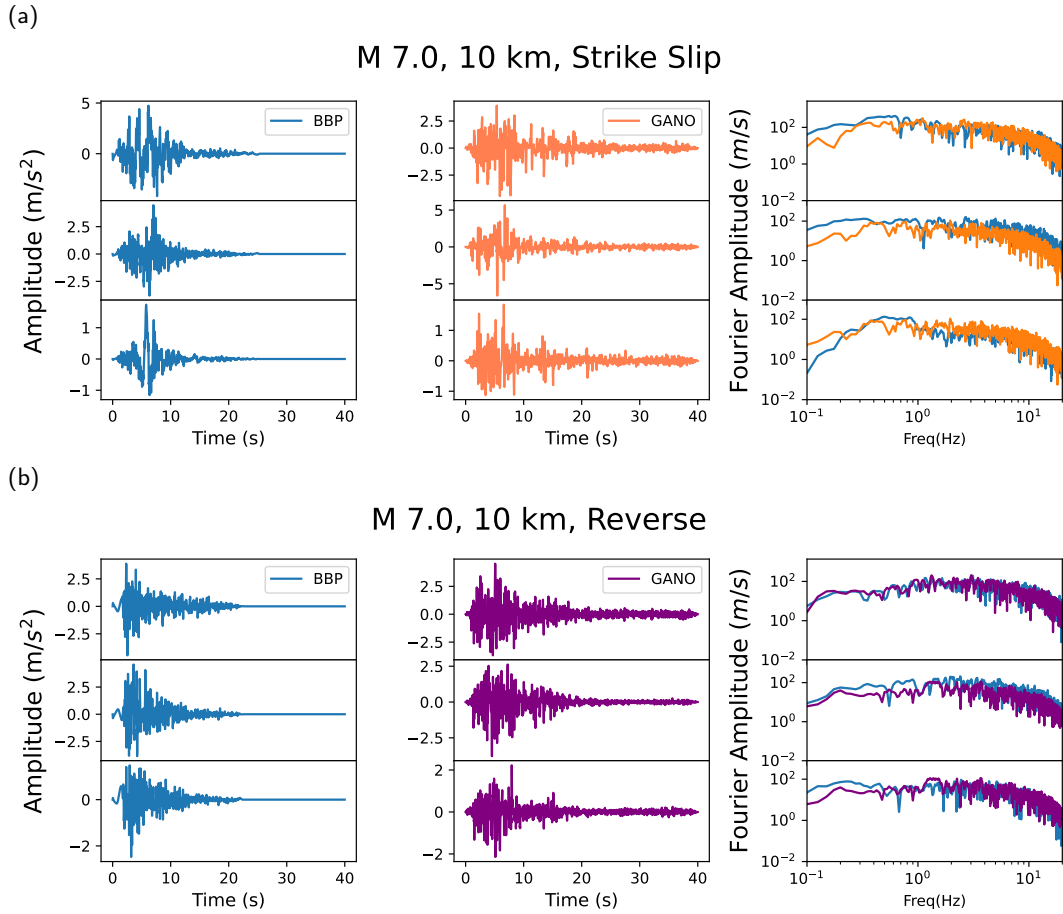


Figure 3: Time-domain and frequency-domain waveforms comparisons of BBP and GANO generated ground motions. Subfigure (a) corresponds to a three-component waveform comparison for $M_w = 7$, $R_{rup} = 10km$, and strike-slip style of faulting. Subfigure (b) corresponds to a three-component waveform comparison for $M_w = 7$, $R_{rup} = 10km$, and reverse style of faulting.

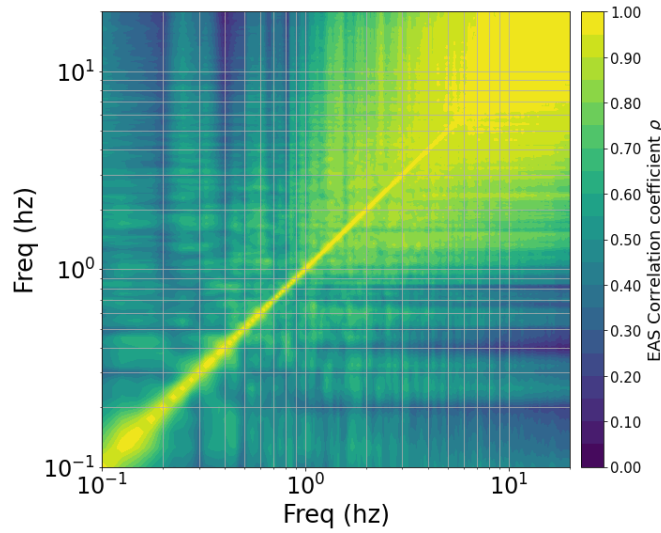


Figure 4: Inter-frequency correlation of synthetically generated ground motions through cGM-GANO based on the BBP training dataset.

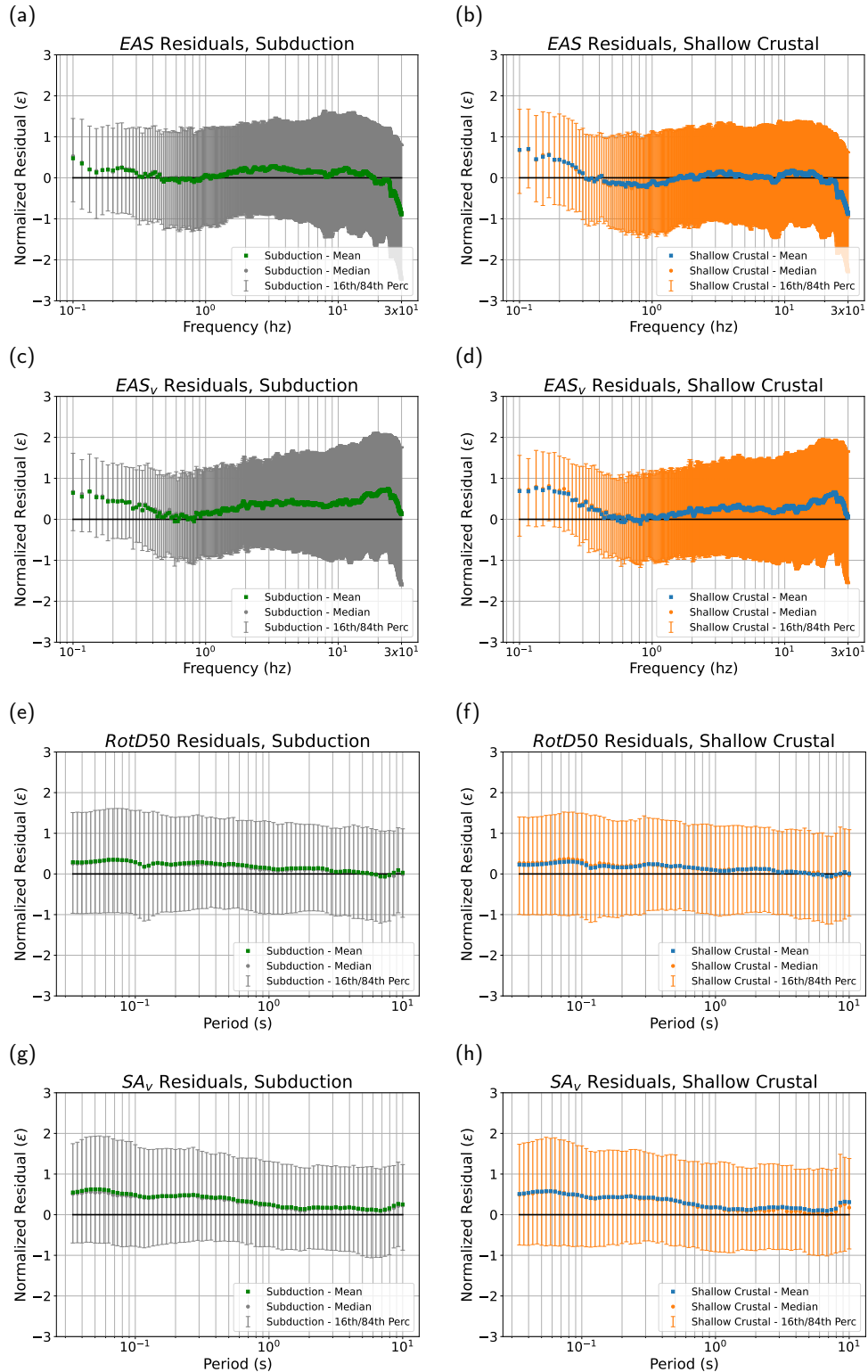
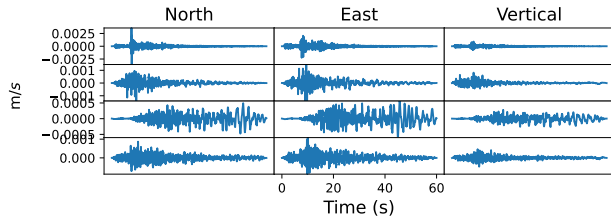
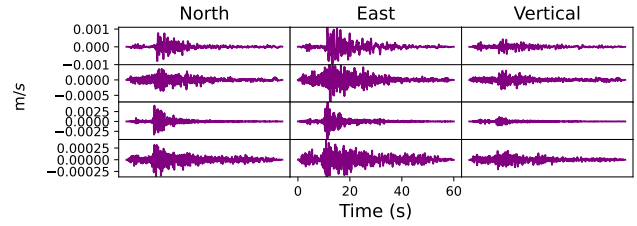


Figure 5: Residual plots of the kik-net trained model based on the validation kik-net dataset (10 % of the total kik-net dataset) . Subfigures (a) and (b) show the horizontal EAS residuals for subduction and shallow crustal events, respectively. Subfigures (c) and (d) show the vertical EAS residuals for subduction and shallow crustal events, respectively. Subfigures (e) and (f) show the horizontal RotD50 PSA residuals for subduction and shallow crustal events, respectively. Subfigures (g) and (h) show the vertical PSA residuals for subduction and shallow crustal events, respectively.

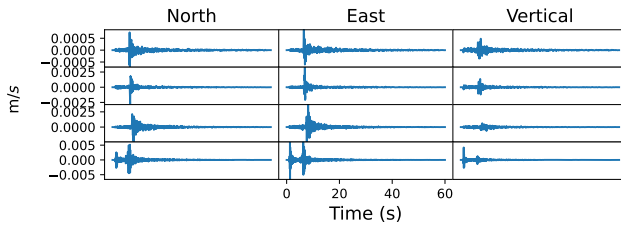
(a) Observation: M 4.5, 50 km, 300 m/s, Shallow Crustal, Velocity



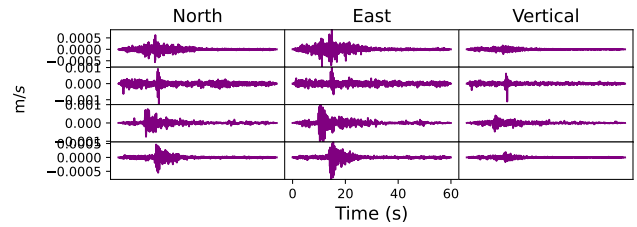
(b) GANO: M 4.5, 50 km, 300 m/s, Shallow Crustal, Velocity



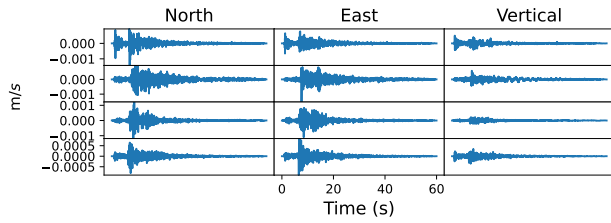
(c) Observation: M 4.5, 50 km, 700 m/s, Subduction, Velocity



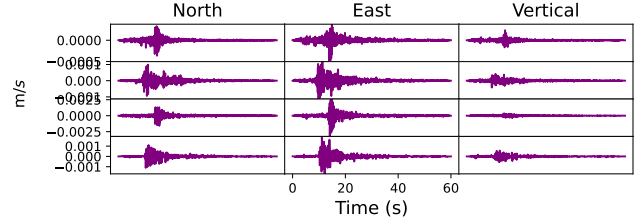
(d) GANO: M 4.5, 50 km, 700 m/s, Subduction, Velocity



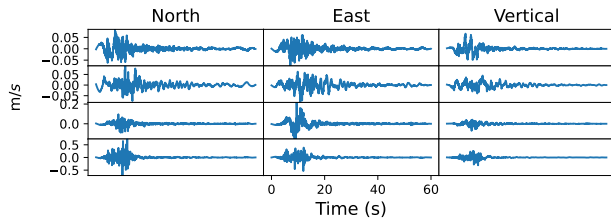
(e) Observation: M 4.5, 50 km, 700 m/s, Shallow Crustal, Velocity



(f) GANO: M 4.5, 50 km, 700 m/s, Shallow Crustal, Velocity



(g) Observation: M 7.2, 20 km, 500 m/s, Shallow Crustal, Velocity



(h) GANO: M 7.2, 20 km, 500 m/s, Shallow Crustal, Velocity

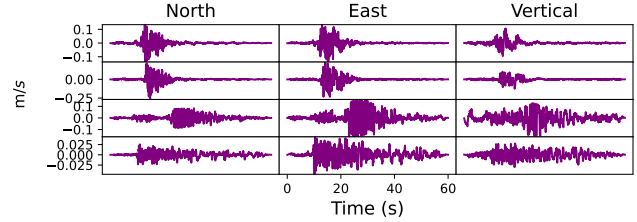


Figure 6: Velocity waveform comparisons between data and synthetic ground motions from cGM-GANO trained on the Kik-net dataset, unit in m/s .

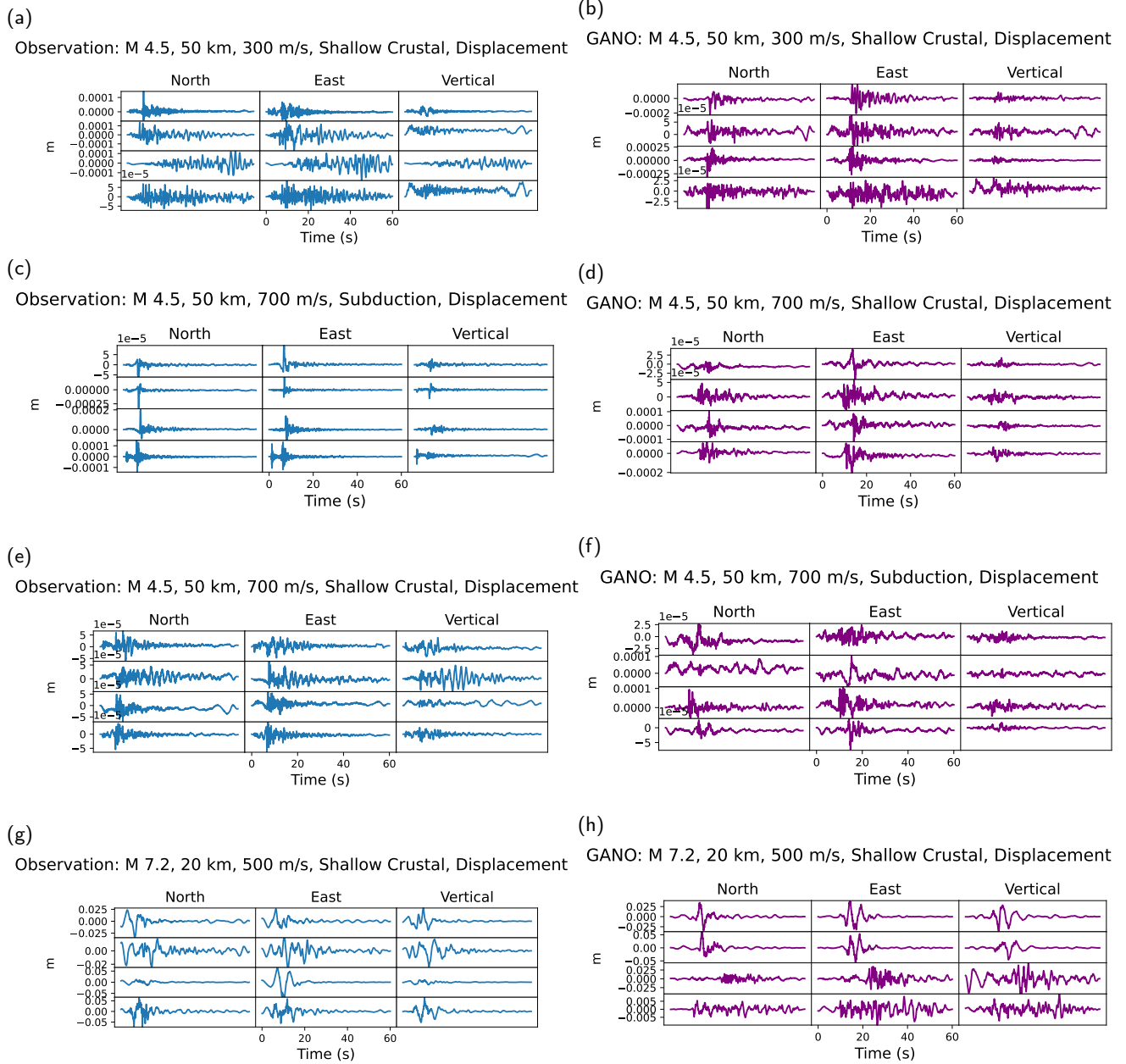


Figure 7: Displacement waveforms comparisons between data and synthetic ground motions from cGM-GANO trained on the Kik-net dataset, unit in m .